



LAWRENCE
LIVERMORE
NATIONAL
LABORATORY

Refraction-Enhanced Backlit Imaging of Axially-Symmetric Inertial Confinement Fusion Plasmas

J. A. Koch, O. L. Landen, L. J. Suter, L. P. Masse, D. S. Clark, J. S. Ross, A. J. Mackinnon, N. B. Meezan, C. A. Thomas, Y. Ping

February 11, 2013

Applied Optics

Disclaimer

This document was prepared as an account of work sponsored by an agency of the United States government. Neither the United States government nor Lawrence Livermore National Security, LLC, nor any of their employees makes any warranty, expressed or implied, or assumes any legal liability or responsibility for the accuracy, completeness, or usefulness of any information, apparatus, product, or process disclosed, or represents that its use would not infringe privately owned rights. Reference herein to any specific commercial product, process, or service by trade name, trademark, manufacturer, or otherwise does not necessarily constitute or imply its endorsement, recommendation, or favoring by the United States government or Lawrence Livermore National Security, LLC. The views and opinions of authors expressed herein do not necessarily state or reflect those of the United States government or Lawrence Livermore National Security, LLC, and shall not be used for advertising or product endorsement purposes.

Refraction-Enhanced Backlit Imaging of Axially-Symmetric Inertial Confinement Fusion Plasmas

**J. A. Koch^{1,*}, O. L. Landen¹, L. J. Suter¹, L. P. Masse², D. S. Clark¹, J. S. Ross¹,
A. J. Mackinnon¹, N. B. Meezan¹, C. A. Thomas¹, Y. Ping¹**

¹Lawrence Livermore National Laboratory, P. O. Box 808, L-493,

Livermore, CA, 94550, USA

²CEA, DAM, DIF, F-91297 Arpajon, France

**Corresponding author: koch1@llnl.gov*

X-ray backlit radiographs of dense plasma shells can be significantly altered by refraction of x-rays that would otherwise travel straight-ray paths, and this effect can be a powerful tool for diagnosing the spatial structure of the plasma being radiographed. We explore the conditions under which refraction effects may be observed, and we use analytical and numerical approaches to quantify these effects for one-dimensional radial opacity and density profiles characteristic of inertial-confinement fusion (ICF) implosions. We also show how analytical and numerical approaches allow approximate radial plasma opacity and density profiles to be inferred from point-projection refraction-enhanced radiography data. This imaging technique can provide unique data on electron density profiles in ICF plasmas that cannot be obtained using other techniques, and the uniform illumination provided by point-like

x-ray backlighters eliminates a significant source of uncertainty in inferences of plasma opacity profiles from area-backlit pinhole imaging data when the backlight spatial profile cannot be independently characterized. The technique is particularly suited to in-flight radiography of imploding low-opacity shells surrounding hydrogen ice, because refraction is sensitive to the electron density of the hydrogen plasma even when it is invisible to absorption radiography. It may also provide an alternative approach to timing shock waves created by the implosion drive, that are currently invisible to absorption radiography.

OCIS codes: 340.7440, 120.5710, 110.1650, 110.2990

I. Introduction

Backlit x-ray radiography has been an important implosion plasma diagnostic at the Nova Laser Facility [1] and at the Omega Laser Facility [2], and it remains an important diagnostic at the National Ignition Facility (NIF) [3,4]. Transmission of backlight x-rays along a chord through a spherically symmetric plasma can be calculated from the line-integrated optical depth that is the forward Abel transform of the radial opacity profile, and so the radial opacity profile can in principle be calculated from radiograph data using a backwards Abel transform of the negative logarithm of the transmission profile. Generalizations to axially-symmetric plasmas are straightforward [5], and more sophisticated back-transforms and forward fits using model opacity profiles can also be applied [3].

These approaches are appropriate when the plasma can be treated as a non-refracting absorbing object, but fail when refraction becomes significant. Refraction effects can become dominant when large density gradients are present in weakly absorbing materials [6-9], and can be important in implosion plasmas [7]. These effects can present data analysis and interpretation challenges, but can also provide rich additional information that straight-ray opacity data cannot provide.

From a diffraction perspective, a light wave from a backlight source experiences a localized phase shift in passing through a semi-transparent object. The transmitted wavefront interferes with itself, and over sufficient propagation distances the phase perturbations generate light intensity perturbations in an image plane. From a geometrical optics perspective, straight rays from the backlight source are refracted by transverse density gradients in the object, and this adds or subtracts light intensity locally

in an image plane. When imaging effects can be understood from a geometrical optics perspective, the analysis generally simplifies significantly, allowing simple formulas to be derived to predict the light intensity pattern [7]. The two perspectives approach equivalence for object spatial scales L , propagation distances q , and light wavelengths λ that correspond to Fresnel numbers $F = L^2/q\lambda$ greater than unity. This refraction-enhanced imaging regime is of interest in fields such as medical imaging [10-13] and astronomy [14], and is generally of greatest interest for inertial confinement fusion (ICF) implosion plasma research [7].

Earlier work [7] began to explore refraction-enhanced radiography of implosion plasmas. Here we systematically investigate the application of the technique and the interpretation of the data, with the goal of evaluating how it can add to our ability to diagnose the spatial structure of implosion plasmas. In Section II, we explore the conditions that must be satisfied for refraction effects to be significant, and we show why point-projection radiography is generally more appropriate for producing refraction-enhanced radiographs than area-backlit pinhole imaging or x-ray microscopy utilizing imaging optics. In Section III, we explore a series of approximations that allow analytical equations to be derived for the refraction-enhanced radiograph profile in terms of the radial opacity and electron density profiles, and in Section IV we show how these radial profiles can in turn be approximately determined from experimental radiographs. In Section V, we show how a least-squares minimization process can be used to infer best-fit model radial opacity profiles from either absorption or refraction-enhanced radiography data profiles, and in Section VI apply the collected results to synthetic data derived from implosion hydrodynamics simulations to infer approximations to both radial

opacity and electron density profiles from single refraction-enhanced radiographs. Finally, in Section VII we summarize the conclusions and potential future impacts of this work.

II. Refraction Enhancements In Implosion Radiographs

The basic concept of refraction-enhanced imaging of implosions was outlined previously [7], and is shown schematically in Figure 1. Fig. 1(a) shows a point-projection backlight geometry, where a ray initially travelling along a straight line from the center of the backlight to the detector with impact parameter b is deviated by a total angle δ , and strikes the detector in a different location. This ray is distinguishable from a straight-ray path when the location where it strikes the detector is outside the magnified image of a spatial resolution element σ , the dimension of which is set by the size of the backlighter W and by the geometry. When δ is small, this condition is approximately,

$$\begin{aligned} q\delta &> \frac{p+q}{2p} \sigma = \frac{p+q}{2p} \frac{q}{p+q} W \\ \delta &> \frac{W}{2p} = \frac{\sigma}{2f} \end{aligned} \tag{1}$$

where p is the backlight/object distance, q is the object/detector distance, and $f = pq/(p+q)$. The solution for δ for a simple $1/r^2$ form of the index of refraction $n(r)$ is given in [7], and we expect the scaling to hold for other simple forms, so we can write the threshold condition for refractive effects to begin to become important given a non-zero backlight size as,

$$\delta = \frac{\pi b}{4} \frac{dn}{dr} \Big|_b = \frac{b r_e \lambda^2}{8} \frac{dN_e}{dr} \Big|_b > \frac{\sigma}{2f}$$

$$r \frac{dN_e}{dr} > \frac{4\sigma}{f r_e \lambda^2}$$
(2)

where we set $b \sim r$, and we use the plasma form for the refractive index $n(r) = 1 - r_e \lambda^2 N_e(r)/2\pi$, with r_e being the classical electron radius, λ being the backlight wavelength, and N_e being the effective free electron density (free or bound with binding energies much less than the backlight x-ray energy; complications to this simple picture are discussed in Section VII). Density gradients that meet this condition do not necessarily produce observable refraction effects, but this approach allows for comparison to other kinds of imaging geometries as discussed below. A detailed analysis of radiograph profiles in the presence of refraction will be presented in Section III.

Fig. 1(b) shows an area-backlit geometry using a pinhole as an imaging element. Here, the bent ray path is distinguishable from the straight path when the ray, projected back to the backlight, begins to fall outside the area of the backlight, the dimension of which is now set by the desired field of view F .

$$p\delta > \frac{W}{2} = \frac{p+d}{2d} F$$

$$\delta > \frac{p+d}{2pd} F = \frac{F}{2f'}$$
(3)

where d is the object/pinhole distance and $f' = pd/(p+d)$. By analogy with eq. (2), we can write the threshold condition as,

$$r \frac{dN_e}{dr} > \frac{4F}{f' r_e \lambda^2}$$
(4)

We can write both eqs. (2) and (4) in a single instructive form,

$$r \frac{dN_e}{dr} > \frac{4}{r_e \lambda^2 (f / \#)} \quad (5)$$

where the effective $f/\#$ for point projection is found from considering the plasma as a simple lens of diameter σ imaging the backlight onto the detector, and for pinhole imaging is found from considering the plasma as a lens of diameter F imaging the backlight onto the pinhole substrate. We assume here that the backlight is appropriately sized to provide the desired spatial resolution (point projection) or field of view (pinhole imaging). For typical values, constrained by the experimental environment of the NIF and other requirements, of $p \approx 10$ mm, $q \approx 1300$ mm, $d \approx 100$ mm, $\sigma \approx 10$ μ m, and $F \approx 1$ mm, pinhole imaging would therefore be expected to be $F/\sigma \sim 100$ times less sensitive to refraction than point-projection imaging. This sensitivity is generally less than was identified in eq. (26) of [7], but is verified by numerical raytrace calculations for area-backlit imaging of a dense plasma shell. This is apparently traceable to the fact that refraction by a dense shell is localized near the midplane of the plasma, where the angle between the density gradient and the ray from the backlight is very near 90 degrees. Essentially, for nearly every ray that is refracted away from the pinhole, there is another ray coming from another region of the backlight that can replace it by refracting into the pinhole. These rays experience nearly identical refraction and absorption, and are essentially indistinguishable.

Finally, we point out that in Fig. 1(b), we can replace the pinhole with an ideal lens and the arguments leading to eq. (4) still hold. An x-ray microscope, imaging the plasma onto the detector using an area backlight, would therefore be expected to show a similar threshold for refractive effects as a pinhole imager operating with the same field

of view, when the microscope optics subtend an effective solid angle large compared with refractive angular deviations. A microscope using a Rowland-circle backlight geometry, with a small backlight or a small aperture on the Rowland circle [15], would have a much higher susceptibility to refraction, according to eq. (2), while an x-ray microscope with small backlight or small aperture off the Rowland circle would show susceptibility between the two cases depending on the geometry and the size of the backlight.

We see that in general, refractive effects in radiographic data will be far more pronounced when the effective backlight dimensions are small, as is the case for point-projection radiography and for microscope radiography systems utilizing a small Rowland-circle backlight or aperture. They will also be pronounced in coherent collimated beam radiography systems such as synchrotrons, where the small divergence angle effectively replaces the small physical backlight size. Pinhole imagers, and un-apertured microscopes operating with area backlighters, will be relatively insensitive to refractive effects, justifying the neglect of these effects in pinhole-imaging absorption radiography data interpretation [1-4].

III. Analytical Analysis Of Refraction And Absorption By An Axially-Symmetric Plasma

We now explore refractive enhancements in more detail, with the goal of obtaining simple analytical equations describing the radiograph profile of an axially-symmetric plasma produced by a point-like backlight. We will begin by considering the problem from a diffraction point of view, and we will show how this approach leads to a

simple equation describing the main features of a refraction-enhanced radiograph of an implosion plasma in terms of Abel transforms of its radial opacity and electron density profiles. We will then consider improvements to this equation from a geometrical optics point of view, and derive a modified equation that reproduces the results of detailed raytracing as well as Fresnel-Kirchoff diffraction calculations for Fresnel numbers > 1 , and reduces to the simpler equation obtained from a diffraction point of view when certain approximations are satisfied.

Diffraction by a non-absorbing phase object with transmitted (straight-ray) phase shift $\phi(x)$ relative to vacuum varying along the x -axis can be treated through a series of approximations to a solution [16] to the Fresnel-Kirchoff integral for the light transmission function $R(x)$ of a uniform collimated beam as a function of x onto a detector a distance q behind the object,

$$R(x) = 1 - \frac{\lambda q}{2\pi} \frac{d^2\phi}{dx^2} \quad (6)$$

The sign can be verified by consideration of a simple optical lens. Approximations required to obtain this equation include the paraxial approximation, the thin phase object approximation ($\sin\phi \approx \phi$, with no absorption), and the neglect of object spatial frequencies in $\phi(x)$ greater than approximately $1/\sqrt{10\lambda q}$, which also derives from a small-angle approximation. In general, for a finite backlight distance, we can replace q by $f = pq/(p+q)$ and define x in the radiograph to be scaled back to the object through the magnification $(p+q)/p$, taking care to correct as necessary for the actual line-of-sight impact parameter given non-zero b/p . This analysis also assumes that no object spatial frequencies are present that satisfy the Talbot self-imaging conditions [17], or that these

frequencies are blurred by imperfect detector spatial resolution or non-zero source size. Finally, clearly the absolute value of the second term in eq. (6) must be small, since negative transmission functions are not physical; this implies that this analysis is only appropriate for perturbative refractive effects and weak phase contrast.

For a slab of plasma of thickness z and electron density $N_e(x)$ and for backlight wavelengths far from any absorption edges, the phase lags the vacuum phase by $\phi(x) = -r_e \lambda N_e(x) z$ (the negative sign arises because the plasma index of refraction is less than unity). Defining the electron areal density $\rho(x) = N_e(x) z$, eq. (6) becomes,

$$R(x) = 1 + \frac{r_e \lambda^2 f}{2\pi} \frac{d^2 \rho}{dx^2} \quad (7)$$

where the sign can be verified by considering a ball of plasma as a weak negative lens for x-rays. For the purpose of one-dimensional imaging of an axially-symmetric plasma in its midplane, the electron areal density is an Abel transform of a radial electron density distribution $N_e(r)$,

$$\rho(x) = 2 \int_x^\infty \frac{r N_e(r) dr}{\sqrt{r^2 - x^2}} \quad (8)$$

so the transmitted intensity at the detector becomes,

$$R(x) = 1 + \frac{r_e \lambda^2 f}{2\pi} \frac{d^2}{dx^2} \left(2 \int_x^\infty \frac{r N_e(r) dr}{\sqrt{r^2 - x^2}} \right) \quad (9)$$

The analysis leading to eq. (7) neglected absorption, and in the limit of $N_e(x) = 0$, $R(x)$ is simply unity. Neglecting refraction, when uniform absorption is present, the transmission is reduced to $\exp(-\tau)$, where $\tau = \alpha z$ is the optical depth and α is the local absorption coefficient. This suggests that we should write the total transmission function

$T(x) = A(x)R(x)$ to account for the presence of absorption in a simple way using a second Abel transform,

$$T(x) = A(x)R(x) = e^{-2 \int_x^\infty \frac{r\alpha(r)dr}{\sqrt{r^2-x^2}}} \left(1 + \frac{r_e \lambda^2 f}{2\pi} \frac{d^2}{dx^2} \left(2 \int_x^\infty \frac{rN_e(r)dr}{\sqrt{r^2-x^2}} \right) \right) \quad (10)$$

The first term $A(x)$ is the absorption radiograph profile considered previously [1-4] in connection with pinhole-based imagers and area backlights, and the second term $R(x)$ is the refractive correction that is most important for point-projection backlighting. When both absorption and refraction are weak, we can approximate the exponential in eq. (10) as $1-t$, so that the net first-order intensity variations of both refraction and absorption simply add [16]. Eq. (10) is therefore appropriate for conditions where both refraction and absorption are small; corrections providing for more accurate treatment of absorption could be included [18,19], but instead we will pursue a more generally accurate equation to replace eq. (10) for forward calculations of radiograph profiles without restricting absorption.

We can test eq. (10) using model $\alpha(r)$ and $N_e(r)$ profiles, and compare the results to what we obtain from numerical raytracing based on an earlier code [20] that was modified to allow smoothly varying refractive index profiles. The raytrace does not rely on paraxial or thin-object approximations, and will become increasingly exact for spatial frequencies less than $1/\sqrt{\lambda f}$, corresponding to a Fresnel number of 1. The code has been tested extensively and does not rely on any of the analytical results of this work, instead it uses essentially eq. (24) of [7] to map the ray path in one dimension through an axially-symmetric plasma having $\alpha(r)$ and $N_e(r)$ profiles specified on a radial grid and interpolated to arbitrary values of r using cubic splines. The source size and source and

detector distances are arbitrary, and typically several million rays are traced to build up an image from a binned histogram in the detector plane.

Figure 2(a) shows model $\alpha(r)$ (for $E = 10$ keV x-ray energy, typical of energies required to penetrate implosion plasmas at the NIF [3,4]) and $N_e(r)$ profiles we use as a first test of eq. (10). These were created by spatially smoothing $\alpha(r)$ and $N_e(r)$ curves from a one-dimensional implosion hydrodynamics simulation with a $5 \mu\text{m}$ full-width at half-maximum (FWHM) Gaussian blur function, in order to damp high spatial frequencies that would not be expected to be accurately captured by eq. (10) given the requirement that $R(x)$ must be close to unity. The details of this particular simulation are not important here; analysis of specific implosion simulation scenarios will be presented in Section VI. The $\alpha(r)$ profile peaks at a larger radius than the $N_e(r)$ profile because the shell is doped plastic plasma surrounding hydrogen-isotope plasma created from cryogenic ice [21], and the inner layers of plastic and hydrogen ice have low x-ray opacity but high electron density. Fig. 2(b) shows radiograph profiles calculated by eq. (10) [22] and simulated with numerical raytracing, assuming $E = 10$ keV and $f = 10$ mm; the choice of f is limited primarily by NIF facility constraints, and we will use these values of E and f throughout the remainder of the paper. In general the radiograph from eq. (10) is a good approximation to the raytrace refraction-enhanced radiograph, but small amplitude differences and peak offsets are evident near the highest peaks and the lowest dips.

To explore these discrepancies further, in Figure 3(a) we show a second set of model $\alpha(r)$ and $N_e(r)$ profiles, created by spatially smoothing $\alpha(r)$ and $N_e(r)$ curves from the same one-dimensional implosion hydrodynamics simulation, but now with a $1 \mu\text{m}$

FWHM Gaussian blur function. These curves maintain high spatial frequencies that exceed the range of applicability of eq. (10), but are still sufficiently low that a raytrace treatment is expected to be adequate for most of the radiograph. Fig. 3(b) shows radiograph profiles calculated by eq. (10) and simulated with numerical raytracing. Refractive effects are now a large perturbation on the absorption-alone radiograph, and would therefore be expected to be crudely approximated by eq. (10). Fig. 3(b) confirms this, with the minimum dip in the raytrace radiograph remaining (as required) above zero, and with structure in the vicinity of the sharpest and highest peaks being distorted and shifted by eq. (10) with respect to those predicted by raytracing.

We can introduce corrections to eq. (10) that essentially exactly reproduce the raytrace radiograph profiles in Figs. 2(b) and 3(b), and that essentially exactly reproduce numerical Fresnel-Kirchoff diffraction calculations except near the sharpest spikes, but these are obtained more easily from a geometrical optics perspective rather than from the diffraction perspective that led to eq. (6). Building on Section III of [7] and following Fig. 4, a ray incident on a surface defined by $s(x)$ in a material with index of refraction $n=1-\epsilon$ and absorption coefficient α will deflect to a final detector position x' , where $x' = x - \epsilon(q + \epsilon s/(1 - \epsilon))(ds/dx)$ to first order in $\epsilon(ds/dx)$. The path length through the object is $s\sqrt{1 + (\epsilon/(1 - \epsilon))^2(ds/dx)^2}$, and to first order in $\epsilon(ds/dx)$ this is simply s . If the incident intensity is I_0 and we keep only first-order terms in $\epsilon(ds/dx)$, then the final transmitted intensity I/I_0 at x' can be calculated using a Jacobean [7] as,

$$T\left(x - \epsilon\left(q + \frac{\epsilon s}{(1 - \epsilon)}\right)\frac{ds}{dx}\right) = \frac{e^{-\alpha s}}{\left|1 - \epsilon\left(q + \frac{\epsilon s}{(1 - \epsilon)}\right)\frac{d^2 s}{dx^2}\right|} \quad (11)$$

where the absolute value follows from the need for $\Delta x'$ to be positive. If we also assume $\varepsilon \ll 1$ and neglect terms involving ε^2 , we have,

$$T\left(x - \varepsilon q \frac{ds}{dx}\right) = \frac{e^{-\alpha s}}{\left|1 - \varepsilon q \frac{d^2 s}{dx^2}\right|} \quad (12)$$

When we set $\varepsilon(ds/dx)$ equal to zero and keep only the leading-order term in $\varepsilon q d^2 s/dx^2$, eq. (12) reduces to $T(x) \sim \exp(-\alpha s)(1 + \varepsilon q d^2 s/dx^2)$. This is exactly analogous to eq. (10), which was derived from a diffraction perspective. Here we find, from a much simpler geometrical optics perspective, that there are amplitude and shift corrections to eq. (10) involving the non-zero first derivative $\varepsilon(ds/dx)$.

We can generalize eq. (12) to phase objects by replacing εs by $-\lambda f/2\pi$, and we can replace q by f to include point-projection backlight geometries. With $\tau(x)$ being the straight-ray optical depth, eq. (12) becomes,

$$T\left(x + \frac{\lambda f}{2\pi} \frac{d\phi}{dx}\right) = \frac{e^{-\tau(x)}}{\left|1 + \frac{\lambda f}{2\pi} \frac{d^2 \phi}{dx^2}\right|} \quad (13)$$

Eq. (13) is quite general, and describes the point-projection intensity pattern produced by an absorbing and phase-shifting object in one dimension, in the geometrical optics limit and to first order in $(\lambda/2\pi)d\phi/dx$. It can also be derived from the Fresnel-Kirchoff integral without limitations on $d\phi/dx$ or $d^2\phi/dx^2$ [23]. In x-ray radiography cases we are interested in, $\phi = -r_e \lambda \rho$, with $\rho(x)$ and $\tau(x)$ being the Abel transforms of $N_e(r)$ and $\alpha(r)$, respectively. This yields,

$$T(x') = T\left(x - \frac{r_e \lambda^2 f}{2\pi} \frac{d\rho(x)}{dx}\right) = \frac{e^{-\tau(x)}}{\left|1 - \frac{r_e \lambda^2 f}{2\pi} \frac{d^2\rho(x)}{dx^2}\right|} \quad (14)$$

Eq. (14) effectively replaces eq. (10), while relaxing the requirements that $d\rho/dx$ be negligibly small and that the $d^2\rho/dx^2$ term be retained only to leading order. It differs from eq. (10) in two significant ways; the right-hand side has the form $1/|1 - d^2\rho/dx^2|$ rather than $(1 + d^2\rho/dx^2)$, and it describes the radiograph intensity not at x but at x' , which is shifted from x by an amount that scales with $d\rho/dx$.

Eq. (14) can be solved numerically for arbitrary $\alpha(r)$ and $N_e(r)$ radial profiles. Figures 5(a) and 5(b) show comparisons between the results of eq. (14) and numerical raytrace calculations, for the $\alpha(r)$ and $N_e(r)$ profiles shown in Figs. 2(a) and 3(a), respectively. Eq. (14) essentially duplicates the raytrace results in both cases, even near the sharpest spikes ($\sim 0.25 \mu\text{m}$ spatial scales) in Fig. 5(b) when one recognizes that eq. (14) becomes singular and forms caustics while the raytrace sums the intensities in a histogram with non-zero bin widths. This occurs when $(r_e \lambda^2 f / 2\pi) d^2\rho/dx^2$ exceeds unity, in which case the intensity at x' becomes the sum of intensities from multiple values of x . In these regions of the radiograph profile, the utility of a geometrical optics perspective becomes questionable, because from a diffraction perspective these least-time paths will interfere and produce oscillatory intensities not captured by a geometrical optics treatment.

We can also check eq. (14) against a brute-force numerical Fresnel-Kirchoff diffraction calculation [7,16,18] with the only approximation being $\lambda\phi(x)/2\pi \ll f$ (so that the fields just past the object are calculated without intermediate steps within the object),

using the same $\alpha(r)$ and $N_e(r)$ profiles shown in Figs. 2(a) and 3(a). These profiles are shown in Figures 6(a) and 6(b), respectively. We see that eq. (14), and therefore the raytrace calculation, is an excellent approximation to the full diffraction calculation except very near the sharpest spikes in Fig. 6(b), where again we would expect a geometrical optics treatment to be inadequate. This validates both improvements in eq. (14) over eq. (10); in general, eq. (13) is a significant improvement over eq. (6) when radiographing objects where $\tau(x)$ and $(\lambda/2\pi)d^2\phi/dx^2$ are not necessarily small and where $(\lambda/2\pi)d\phi/dx$ cannot be neglected, and remains accurate throughout the geometrical optics regime of Fresnel numbers > 1 [23].

Analytical solutions to eq. (14) for $T(x)$, rather than $T(x')$, could be pursued, but we do not pursue them here for two reasons. First, our goal is to obtain a relatively simple equation that describes the main features of point-projection radiographs of in-flight NIF implosions, and that can be inverted to allow $\alpha(r)$ and $N_e(r)$ profiles to be obtained from radiographic data, and inversion of eq. (14) seems intractable. Second, in a real implosion plasmas we expect that the sharp gradients found in ideal one-dimensional implosion hydrodynamics simulations will be smoothed over small solid angles by three-dimensional instability growth, with effective chord-integrated interface thicknesses of 5-10 μm [24]. In practical terms, there is little justification for analytical developments of eq. (14) given the mathematical complexity and given the limitations of NIF implosion diagnostic capabilities, and as a corollary there is likely no benefit to developing imaging systems capable of better than $\sim 5\text{-}10\ \mu\text{m}$ object resolution for side-on in-flight implosion radiography applications. Eq. (14) is a significant improvement over eq. (10) when sub-10- μm resolution data is obtained with excellent signal-to-noise,

particularly for objects that have μm -scale radial density features. Improved accuracy could be important for diagnosis of interface instability growth very early in the implosion, or for diagnosis of shock propagation before the interfaces have moved significantly [25], in which case eq. (14), rather than eq. (10), should be used in iterative numerical forward fits using model $\alpha(r)$ and $N_e(r)$ profiles.

We find that in general, a radiograph profile of an absorbing plasma characterized by $\alpha(r)$ will be modified by additional peaks and dips arising from radial variations in $N_e(r)$, and that these peaks and dips may be enhanced or suppressed according to the scale factor $f\lambda^2$. These peaks and dips will be suppressed in a pinhole imaging system, compared with a point-projection system, by factors estimated from eq. (5) to be ~ 100 , justifying the neglect of refractive effects in the analysis of implosion radiographs obtained with pinhole and slit imagers [1-4]. Refractive enhancements are expected to be significant in point-projection imaging of implosions at the NIF, and for many purposes these enhancements are well-described by eq. (10) that multiplies the absorption-only radiograph profile by a refraction term involving the second derivative of the Abel transform of the $N_e(r)$ profile. Where eq. (10) begins to fail, when density profiles with sharp gradients are imaged with high spatial resolution, eq. (14) essentially exactly reproduces a full raytrace calculation, and essentially exactly reproduces a numerical Fresnel-Kirchoff calculation throughout the geometrical optics regime, at the cost of greater complexity and an inability to invert radiograph profiles to obtain radial profiles. While refraction enhancements would complicate an absorption-only interpretation that is already well-developed [3,4], here we exploit these enhancements to provide additional

information on implosion plasma structure that cannot be obtained from conventional absorption radiographs.

IV. Inference of Electron Density Profiles From Refraction Radiography Data

In this section we show how approximate plasma electron density profiles $N_{\text{eff}}(r)$ can be obtained from refraction-enhanced radiographs when absorption is negligible, or when the absorption-only radiograph profile is known independently, e.g. from simultaneous area-backlit pinhole image data taken along a nearby line of sight. This analysis relies on a backwards inversion [26] of eq. (10). While eq. (10) is an approximation to the (non-invertible) eq. (14), we will show that for most qualitative and quantitative purposes in ICF plasma diagnosis, the approximation is adequate.

To zero-order in the derivative dp/dx , the total radiograph profile is the product of the absorption part $A(x)$ and the refraction part $R(x)$, so when $A(x)$ is unity (negligible absorption) we can write eq. (10) as,

$$R(x) = 1 + \frac{r_e \lambda^2 f}{2\pi} \frac{d^2}{dx^2} \left(2 \int_x^\infty \frac{r N_e(r) dr}{\sqrt{r^2 - x^2}} \right) \quad (15)$$

and, therefore,

$$\left(2 \int_x^\infty \frac{r N_e(r) dr}{\sqrt{r^2 - x^2}} \right) = \frac{2\pi}{r_e \lambda^2 f} \int_0^x dx' \int_0^{x'} dx'' (R(x'') - 1) \quad (16)$$

Eq. (16) has the form of an Abel transform,

$$f(x) = \bar{A}(g(r)) \quad (17)$$

which implies that it can be inverted by an Abel back-transform,

$$g(r) = \bar{A}^{-1}(f(x)) = \frac{-1}{\pi} \int_r^\infty dx \frac{\left(\frac{df(x)}{dx} \right)}{\sqrt{x^2 - r^2}} \quad (18)$$

Therefore, we can invert eq. (16) to obtain,

$$N_e(r) = \frac{-2}{r_e \lambda^2 f} \int_r^\infty dx \frac{\left(\int_0^x dx' (R(x') - 1) \right)}{\sqrt{x^2 - r^2}} \quad (19)$$

When $R(x)$ is blurred in radiograph space, e.g. by non-zero backlight size or imperfect detector spatial resolution, then eq. (19) assumes the point-spread function has been deconvolved; we return to this issue in Section VI. Abel back-transforms are well-known to amplify absorption radiograph data noise [3], but here the back-transform involves an integral over data in the numerator of the integrand, rather than a derivative. This makes the process relatively insensitive to noise in the refraction radiograph data.

In practice, we cannot obtain radiograph data over the full $[0, \infty]$ range of x , but instead we obtain data within a window $[a, b]$; this constraint is imposed by the requirements of practical point-projection radiography geometries at the NIF, particularly the need for high magnification imaging of a single limb of the implosion. This necessitates additional constraints and approximations to obtain $N_e(r)$. Defining $S(x) = R(x) - 1$, we write,

$$N_e(r) = \left[\frac{-2}{r_e \lambda^2 f} \right] \left[\int_r^b dx \frac{\left(\int_0^a S(x') dx' + \int_a^x S(x') dx' \right)}{\sqrt{x^2 - r^2}} + \int_b^\infty dx \frac{\left(\int_0^b S(x') dx' + \int_b^x S(x') dx' \right)}{\sqrt{x^2 - r^2}} \right] \quad (20)$$

We can simplify this by making use of the fact that the integral of $S(x)$ over all x must be zero, since refraction simply shifts rays around at the detector plane. Furthermore, in

practice, for a reasonably wide radiograph window that captures the refractive features of an imploding shell, $S(x)$ falls rapidly to zero near the outer edge of the window, so that we approximate the integral of $S(x)$ on $[0, b]$ as zero and set $S(x) = 0$ for $x > b$. Eq. (20) then becomes,

$$N_{efit}(r) = \left[\frac{-2}{r_e \lambda^2 f} \right] \left[\int_r^b dx \frac{\int_a^x S(x') dx'}{\sqrt{x^2 - r^2}} - S_{int} \ln \left(\frac{b + \sqrt{b^2 - r^2}}{r} \right) \right] \quad (21)$$

$$S_{int} = \int_a^b S(x) dx$$

where $N_{efit}(r)$ is an approximation to the unknown function $N_e(r)$. The first term is eq. (19) over the finite $[a, b]$ radiograph window, and the second term is a radially-dependent correction to approximately account for the finite window.

A potentially more significant correction to real radiograph data is the fact that in general, the radiograph profile has errors due to uncertainties in the baseline backlight brightness level and due to intensity gradients caused e.g. by vignetting of backlit pinholes or slits [27] or by uncertain flat-field corrections in streaked or gated framing camera detectors [3,4]. These uncertainties can be very problematic in area-backlit pinhole data because in general the area backlight spatial profile is not independently known and must be estimated, but for our purposes using a point-like backlight that produces a very uniform backlight intensity profile, we will approximate these corrections as simple offset and slope additions to $S(x)$. Replacing $S(x)$ by $S(x) + A + Bx$, we have,

$$N_{fit}(r) = \left[\frac{-2}{r_e \lambda^2 f} \right] + A \left(\sqrt{b^2 - r^2} - b \ln \left(\frac{b + \sqrt{b^2 - r^2}}{r} \right) \right) + \frac{B}{4} \left(b \sqrt{b^2 - r^2} \right) + (r^2 - 2b^2) \ln \left(\frac{b + \sqrt{b^2 - r^2}}{r} \right) \quad (22)$$

We now assume that the electron density function is effectively zero with zero slope on the inner window boundary $r = a$, which we would expect to be a good approximation to the actual inflight density profile of an imploding shell. This sets boundary conditions on the slope and offset terms, which allows them to be solved as,

$$A = \frac{c_{12}f'(a) - c_{22}f(a)}{c_{11}c_{22} - c_{12}c_{21}} \quad (23)$$

$$B = \frac{c_{21}f(a) - c_{11}f'(a)}{c_{11}c_{22} - c_{12}c_{21}}$$

with the matrix c defined as,

$$\begin{bmatrix} c_{11} & c_{12} \\ c_{21} & c_{22} \end{bmatrix} = \begin{bmatrix} \sqrt{b^2 - a^2} - b \ln \left(\frac{b + \sqrt{b^2 - a^2}}{a} \right) & \frac{1}{4} \left(b \sqrt{b^2 - a^2} + (a^2 - 2b^2) \ln \left(\frac{b + \sqrt{b^2 - a^2}}{a} \right) \right) \\ \frac{\sqrt{b^2 - a^2}}{a} & \frac{1}{2} \left(\frac{b \sqrt{b^2 - a^2}}{a} + a \ln \left(\frac{b + \sqrt{b^2 - a^2}}{a} \right) \right) \end{bmatrix} \quad (24)$$

and $f(a)$ and $f'(a)$ defined as,

$$\begin{aligned}
f(a) &= \left(\int_r^b dx \frac{\int_a^x S(x') dx'}{\sqrt{x^2 - r^2}} \right)_{r=a} - S_{\text{int}} \ln \left(\frac{b + \sqrt{b^2 - a^2}}{a} \right) \\
f'(a) &= \frac{d}{dr} \left(\int_r^b dx \frac{\int_a^x S(x') dx'}{\sqrt{x^2 - r^2}} \right)_{r=a} + S_{\text{int}} \frac{b}{a\sqrt{b^2 - a^2}}
\end{aligned} \tag{25}$$

This is straightforward to solve numerically. The resulting corrections to the $N_{\text{efit}}(r)$ profile are generally valuable even when there are no actual slope and offset errors in the radiograph, because they serve as adjustable parameters to correct any residual errors left in eq. (21) while forcing the solution to satisfy realistic boundary conditions.

Figure 7 shows a comparison between the $N_e(r)$ profile from Fig. 2(a), and the inferred $N_{\text{efit}}(r)$ profile from eqs. (22-25). Here we use the raytrace refraction-only radiograph of the $N_e(r)$ profile in Fig. 2(a) as an input to the backwards analysis that is based on eq. (10), with radiograph window bounds $a = 350 \mu\text{m}$ and $b = 700 \mu\text{m}$. The agreement is excellent, with minor differences near the sharpest peaks of $N_e(r)$ and in the large-radius tail, where eqs. (22-25) force $N_{\text{efit}}(r)$ to zero at the edge of the radiograph window (not shown). Exact agreement can not be obtained, both because the radiograph window does not extend over all values of x and because eq. (10) is an approximation to eq. (14), but for implosion diagnosis purposes the agreement is more than adequate to discern the existence of two peaks in $N_e(r)$, their separation, the peak value of N_e , and the overall width of the $N_e(r)$ profile. These features could never be observed or quantified with conventional absorption radiography, which at best can only recover the $\alpha(r)$ profile in Fig. 2(a) that does not contain these features.

The agreement shown in Fig. 7 becomes less quantitative when absorption is not negligible, and when $R(x)$ must be approximated by dividing $T(x)$ by an $A(x)$ profile determined in another way, either by simultaneous area-backlit pinhole imaging along an equivalent line of sight, or by fitting as will be described in Section V. Figure 8 plots the refraction-only radiograph $R(x)$ of the $N_e(r)$ profile in Fig. 2(a) against $T(x)/A(x)$, where for clarity the curves are now calculated from eq. (14) rather than generated by raytracing. The peaks and dips remain in the correct positions when we approximate $R(x)$ by $T(x)/A(x)$, but their heights and depths change, and these changes would be expected to impact the $N_{\text{effit}}(r)$ profile inferred from eqs. (22-25). Figure 9 confirms this; the $N_{\text{effit}}(r)$ profile inferred from eqs. (22-25) using $T(x)/A(x)$ is qualitatively different from the profile inferred using $R(x)$ in the limit of no absorption (Fig. 7), and qualitatively different from the actual $N_e(r)$ profile.

This occurs because, in eq. (14), the intensity profile at radiograph position x' is determined by the derivatives of the electron density at object position x as well as the optical depth at position x , and in general $x' \neq x$. When absorption is not negligible, small variations on a steeply-sloping absorption radiograph $A(x)$ can affect the denominator of $T(x)/A(x)$, resulting in errors in the inferred $R(x)$ profile. However, the inferred $N_{\text{effit}}(r)$ profile in Fig. 9 remains adequate to discern the existence of two peaks in $N_e(r)$, their separation within $\sim 2 \mu\text{m}$, the peak value of N_e within $\sim 50\%$, and the overall width of the $N_e(r)$ profile (defined as the separation between the outer peaks of $d^2N_e(r)/dr^2$) within $\sim 3 \mu\text{m}$.

We have shown that a back-analysis of refraction-enhanced radiograph data profiles, applying eqs. (22-25) to the refractive part of the radiograph, yields a good

approximation to the actual $N_e(r)$ profile within the plasma. The approximation is very good when absorption is negligible and $T(x)/A(x) = R(x)$, despite the foundation of eqs. (22-25) being eq. (10) rather than eq. (14), and while the correspondence degrades when absorption is not negligible and $T(x)/A(x)$ must be used together with an $A(x)$ curve inferred by other means, the main features of the actual $N_e(r)$ profile are still accurately inferred.

V. Inference of Opacity Profiles From Absorption and Refraction-Enhanced Radiography Data

In the analysis of Section IV, we assumed that the absorption profile $A(x)$ was known independently, e.g. from area-backlit pinhole imaging, so that we could infer an approximation to $R(x)$ by measuring the total refraction-enhanced radiograph $T(x)$ and dividing $T(x)$ by $A(x)$. In this section, we will first develop a forward model fitting procedure that allows accurate $\alpha(r)$ profiles to be extracted from absorption-only radiograph profiles $A(x)$ obtained using area backlighting over a narrow window, when the area backlight has weak spatial non-uniformities. This procedure represents a significant improvement over earlier work [3] when the radiograph is obtained over a window of a single limb of the implosion, and when the $\alpha(r)$ profile is allowed to deviate significantly from a Gaussian functional form by having a power-law tail extending to large radius. We will then generalize this process to allow $A(x)$ and therefore $\alpha(r)$ to be inferred from $T(x)$ without a second radiograph measurement, despite the presence of additional peaks and dips in the $T(x)$ profile caused by refraction. This is particularly valuable because a point-projection radiograph naturally has a very uniform backlight

intensity profile, eliminating potentially large analysis errors introduced by the mapping of area-backlight spatial non-uniformities into the radiographs when pinhole imaging is used.

When refractive effects are negligible (E is large, f is small, $N_e(r)$ gradients are small, or when pinhole imaging over a wide field of view is used), eq. (10) simplifies to a standard absorption radiograph profile,

$$T(x) = A(x) = e^{-2 \int_x^\infty \frac{r\alpha(r)dr}{\sqrt{r^2-x^2}}} \quad (26)$$

So far we have assumed that radiograph profiles are unblurred, or that any spatial blurring has been deconvolved prior to analysis. When we work with raw data radiographs that contain blurring and have up to second-order spatial variations in the backlight baseline profile, we can generalize eq. (26) to,

$$\begin{aligned} A(x) &= \int_{-\infty}^{\infty} e^{-2 \int_{\xi}^{\infty} \frac{r\alpha(r)dr}{\sqrt{r^2-\xi^2}}} G(x-\xi) dy + D + Ex + Fx^2 \\ &\equiv \int_{-\infty}^{\infty} e^{-\tau(\xi)} G(x-\xi) d\xi + D + Ex + Fx^2 \end{aligned} \quad (27)$$

where $G(x)$ is an (assumed known) area-normalized blur function, $\tau(x)$ is the forward Abel transform of $\alpha(r)$, and D , E and F are parameters describing the backlight profile. We now assume an explicit functional form for $\alpha(r)$, which we will justify later by comparison to $\alpha(r)$ profiles derived from implosion hydrodynamics simulations,

$$\begin{aligned} \alpha_{fit}(r) &= Ce^{\frac{-(r-r_0)^2}{\Delta^2}}, \quad r \leq r_0 + \Delta\sqrt{\gamma/2} \\ &= \frac{C \exp(-\gamma/2) \left(\Delta\sqrt{\gamma/2}\right)^\gamma}{(r-r_0)^\gamma}, \quad r > r_0 + \Delta\sqrt{\gamma/2} \end{aligned} \quad (28)$$

Here $\alpha_{\text{fit}}(r)$ is assumed to be Gaussian out to a cut-off radius, at which point the functional form changes to a decaying power law while matching function values and derivatives across the boundary. The power-law tail is expected to be an important feature of the actual $\alpha(r)$ profile, particularly at late times during the implosion when the shell has nearly burned through and the ablated plasma contains significant mass and opacity [4]. Here we differ from other approaches to analyzing area-backlit pinhole image data [3], which model the opacity profile with a Gaussian function.

We can now treat eq. (27), with $\alpha_{\text{fit}}(r)$ described by eq. (28), as a fit function $A_{\text{fit}}(x)$ to an actual absorption radiograph $y(x)$, and we can adjust the values of the seven parameters (D, E and F describing the backlight, and C, D, r_0 and γ describing the $\alpha(r)$ profile) to minimize a fit metric χ^2 , where,

$$\chi^2 \equiv \sum_{i=1}^N W_i^2 \left(y_i - A_{\text{fit}}(x_i; D, E, F, C, \Delta, r_0, \gamma) \right)^2 \quad (29)$$

where x_i , y_i are the radiograph points from $i = 1$ to N and W_i are weight values. χ^2 is minimized locally when the derivatives of χ^2 with respect to the parameters are all zero. The resulting equations are intractable, so we use Newton's method to simultaneously solve them iteratively using first and second derivatives of χ^2 . Starting from initial guesses, and damping the changes between iterations by a factor $\delta < 1$ to eliminate instability, the $(j+1)$ iteration of these equations can be written as,

$$\begin{aligned}
D_{j+1} &= D_j + \frac{\delta \sum_i W_i^2 (y_i - A_{\text{fit}}(x_i))}{\sum_i W_i^2} \\
E_{j+1} &= E_j + \frac{\delta \sum_i W_i^2 (y_i - A_{\text{fit}}(x_i)) x_i}{\sum_i W_i^2 x_i^2} \\
F_{j+1} &= F_j + \frac{\delta \sum_i W_i^2 (y_i - A_{\text{fit}}(x_i)) x_i^2}{\sum_i W_i^2 x_i^4} \\
P_{j+1} &= P_j + \frac{\delta \sum_i W_i^2 (y_i - A_{\text{fit}}(x_i)) \left[\int \frac{d\tau_j(\xi)}{dp} e^{-\tau_j(\xi)} G(x_i - \xi) d\xi \right]}{\sum_i W_i^2 \left((y_i - A_{\text{fit}}(x_i)) \left[\int \left(\frac{d\tau_j(\xi)}{dp} \right)^2 e^{-\tau_j(\xi)} G(x_i - \xi) d\xi - \int \frac{d^2 \tau_j(\xi)}{dp^2} e^{-\tau_j(\xi)} G(x_i - \xi) d\xi \right] - \left[\int \frac{d\tau_j(\xi)}{dp} e^{-\tau_j(\xi)} G(x_i - \xi) d\xi \right]^2 \right)}
\end{aligned} \tag{30}$$

where $A_{\text{fit}}(x)$ is given by eq. (27), and p is any parameter of $\alpha(r)$ in eq. (28), i.e. C , D , r_0 or γ . With $\alpha_{\text{fit}}(r)$ given by eq. (28), the derivatives of $\tau(x)$ can be written analytically as Abel transforms of derivatives of $\alpha(r)$, and solved numerically in the same way [22]. For fitting to absorption radiographs, we set all $W_i = 1$.

We now explore the ability of eq. (30) to correctly infer an opacity profile described by eq. (28) when the input radiograph is generated from an opacity profile having this same analytical form. Figure 10 shows an analytical $\alpha(r)$ profile from eq. (28) with $C = 0.004 \text{ } \mu\text{m}^{-1}$, $D = 10 \text{ } \mu\text{m}$, $r_0 = 482 \text{ } \mu\text{m}$, and $\gamma = 0.9$, and its unblurred absorption radiograph $A(x)$ together with the best-fit radiograph $A_{\text{fit}}(x)$ and inferred $\alpha_{\text{fit}}(r)$ profile obtained using eq. (30) assuming no blurring ($G(x)$ is a delta function). For fitting the calculated radiograph, we use radiograph window bounds of $a = 375 \text{ } \mu\text{m}$ and $b = 625 \text{ } \mu\text{m}$, and we extend the Abel transform integrals to $R = b + (b - r_0)$ in $\tau(x)$ using the fit $\alpha_{\text{fit}}(r)$ function in order to approximately account for opacity outside the radiograph window (the Abel integrals diverge for $\gamma \leq 1$, and in any case a real plasma $\alpha(r)$ profile must drop to zero beyond a radius containing all the initial mass). For practical purposes,

the agreement in both $\alpha(r)$ and $A(x)$ is perfect; eq. (30) exactly infers the correct $\alpha(r)$ profile given its windowed radiograph as an input and then fitting in $A(x)$ space.

We can repeat the calculation leading to Fig. 10, but using an input radiograph profile that is blurred with a 20 μm FWHM Gaussian function and then fitting it to a blurred profile, with $G(x)$ in eq. (30) being a 20 μm FWHM Gaussian. Figure 11 shows the results, again yielding essentially exact agreement in both $\alpha(r)$ and $A(x)$. Finally, we can repeat the same calculation again, using a 20 μm FWHM-blurred radiograph profile that is deliberately offset by a second-order backlight profile ($D = 0.0875$, $E = -7.5 \times 10^{-5}$, $F = -2.5 \times 10^{-7}$ in eq. (27)), and then randomized with Gaussian statistical noise having a standard deviation of 0.03 per 0.1- μm pixel, corresponding to a signal-to-noise ratio of ~ 15 per pixel. The results are shown in Figure 12, and again nearly exact agreement is obtained for both $\alpha(r)$ and $A(x)$. Different statistical realizations of noise yield slightly different inferred $\alpha_{\text{fit}}(r)$ profiles, with variations on the order of the differences shown in Fig. 12.

Having demonstrated the ability of eq. (30) to extract a best-fit $\alpha_{\text{fit}}(r)$ profile according to eq. (28), despite the presence of (known) blurring, non-uniform backlight profiles described by second-order polynomials, and statistical noise, we return to the $\alpha(r)$ profile derived from implosion hydrodynamics simulations and shown in Fig. 2(a). The absorption radiograph profile $A(x)$ shown in Fig. 2(b) is reproduced with an expanded scale in Figure 12, and we also show the best-fit radiograph profile $A_{\text{fit}}(x)$ derived from eq. (30) and the corresponding best-fit $\alpha_{\text{fit}}(r)$ profile. We see that the model $\alpha_{\text{fit}}(r)$ profile of eq. (28) (in this case with $C = 0.0041 \mu\text{m}^{-1}$, $D = 8.4 \mu\text{m}$, $r_0 = 481.5 \mu\text{m}$,

and $\gamma = 0.89$) is well-matched to the actual $\alpha(r)$ profile derived from hydrodynamics simulations, justifying the use of eq. (28). We will show in Section VI that eq. (28) is well-matched to actual $\alpha(r)$ profiles derived from hydrodynamics simulations over a wide range of times during the implosion.

We now show that we can extract a good approximation to $\alpha(r)$ using the model profile of eq. (28) and the fit procedure of eq. (30), but applied to refraction-enhanced radiographs rather than to absorption-only radiographs. This is effective because, away from the peaks and dips caused by refraction through steep density gradients, the refraction-enhanced radiograph rapidly converges to the absorption-only radiograph. Essentially, where the derivative and second derivative of $\rho(x)$ can be neglected in eq. (14), the result is $T(x) = A(x)$. We can therefore fit the refraction-enhanced radiograph in a way that heavily weights the points in regions where negligible refraction is expected, and de-weights the points in regions of significant refractive peaks, dips and shifts. We do this by setting $W_i \ll 1$ in eq. (30) within a region of the refraction-enhanced radiograph defined by inner and outer windows, outside of which we assume $T(x) = A(x)$ and $W_i = 1$.

The raytrace refraction-enhanced radiograph profile shown in Fig. 2(b) is reproduced with an expanded scale in Figure 14 together with the actual $\alpha(r)$ profile from Fig. 2(a). Choosing a de-weighting window of $x = 435\text{-}520 \mu\text{m}$, within which we set $W_i = 0.05$, we find that eq. (30) provides an excellent fit to the absorption part of the radiograph, and that the best-fit $\alpha_{\text{fit}}(r)$ profile (in this case with $C = 0.0038 \mu\text{m}^{-1}$, $D = 9.4 \mu\text{m}$, $r_0 = 481.6 \mu\text{m}$, and $\gamma = 0.82$) is essentially as good as the best-fit profile of Fig. 10 that was inferred from the absorption-only radiograph. This result is typical, as we will

show in Section VI. The choice of $W_i = 0.05$ within the de-weighting window, as well as the choice of the de-weighting window boundaries, is somewhat arbitrary, but generally follows the prescription that the window boundaries should be away from refractive peaks and dips, and that the de-weighting factor should be small but not zero in order to avoid best-fit radiograph solutions that do not go through the radiograph region containing the peaks and dips.

In this section we have developed a numerical analysis procedure that is capable of extracting best-fit $A_{\text{fit}}(x)$ and $\alpha_{\text{fit}}(r)$ profiles from either absorption-only or refraction-enhanced radiographs, according to the model profile of eq. (28), despite the presence of known radiograph blurring, second-order non-uniformities in the backlight profile, and numerical noise. In the next section, we will apply these results together with the back-analysis procedure developed in Section IV to infer $\alpha_{\text{fit}}(r)$ and $N_{\text{efit}}(r)$ profiles from refraction-enhanced radiographs obtained over a range of times during a NIF implosion.

VI. Application to Synthetic NIF Implosion Radiograph Data

In the previous sections, we have developed the capability to infer approximate $\alpha_{\text{fit}}(r)$ (from eq. (30)) and $N_{\text{efit}}(r)$ (from eqs. (22-25)) profiles from refraction-enhanced radiographs of shell plasmas. Neither process is sensitive to data noise ($\alpha_{\text{fit}}(r)$ is inferred from a forward fit using a model function, $N_{\text{efit}}(r)$ is inferred from an Abel back-transform of a double integral that damps noise rather than amplifies it), or to second-order or first-order variations in backlight intensity, respectively. We have also shown that $\alpha(r)$ can be inferred correctly even from data with known spatial blurring, by fitting in blurred radiograph space and extracting an unblurred $\alpha(r)$ function. We now explore

how well these processes work with synthetic radiograph data derived from a specific realistic implosion hydrodynamics simulation, and we quantify the accuracy expected for measurement of several important implosion performance metrics.

For these tests, we use the results of a one-dimensional Hydra [28] simulation of a NIF cryogenic implosion [21]. In this simulation, a Si-doped plastic shell surrounding cryogenic deuterium-tritium ice was imploded with 1.45 MJ of laser energy in a shaped drive tuned to ignite the main fuel at the time of peak compression and central pressure, approximately 22 ns after the start of the laser drive. This capsule differs from the capsule used in the simulations analyzed in Sections III-V, which was doped with Ge at different levels and driven differently; we use the Si-doped design here primarily because it shows reduced opacity at 10 keV, making the analysis process described in Section IV more accurate.

We are interested here in times between 19 and 21 ns, when the capsule is still imploding and when the final fuel configuration is being determined by shock timing, symmetry, ablation pressure, and other physics. At early times, radiograph data analysis becomes challenging because gradients are steep and eq. (10) is no longer a good approximation to eq. (14), while at late times motion blurring within realistic gate time windows degrades the visibility of the refraction features of $T(x)$. We will discuss the former issue in Section VII.

We take four simulated snapshot $\alpha(r)$ and $N_e(r)$ profiles during the implosion, at 19.3, 19.9, 20.4 and 20.8 ns, smooth them with a 5 μm FWHM Gaussian function to approximate chord integration along the diagnostic line of sight, use eq. (14) to generate simulated refraction-enhanced radiographs $T(x)$ from $\alpha(r)$ and $N_e(r)$ extending out to radii

> 2 mm, blur the resulting radiographs with an additional Gaussian function (6.6, 8.8, 10.4 and 11.9 μm FWHM Gaussian, respectively) to approximate the effects of a realistic 5 μm backlight source size [9] and motional blurring within a realistic 40 ps gate time window, and then clip the resulting radiographs with a 250 μm -wide window centered approximately on the center of the imploding shell. We then apply the methodology of Section V to infer the absorption part of the radiograph $A_{\text{fit}}(x)$ and the unblurred $\alpha_{\text{fit}}(r)$ profile, and then apply the methodology of Section IV to the quotient $T(x)/A_{\text{fit}}(x)$ to obtain $N_{\text{efit}}(r)$. We note that blurring of the refractive part of $T(x)$ remains, and so the $N_{\text{efit}}(r)$ profile inferred from the backwards analysis of Section IV will show the effects of this blurring. An alternative approach would be to deconvolve the known blurring from $T(x)$, infer the unblurred $A_{\text{fit}}(x)$ from the forward fit procedure, and then infer the unblurred $N_{\text{efit}}(r)$. When spatial blurring is larger, this process could be preferable despite the additional errors and uncertainties it would introduce, but for present purposes we will show that it is unnecessary.

Figures 15(a)-15(d) show the synthetic radiographs $T(x)$ and $A(x)$ (the latter is not used in this analysis) obtained from the above processing of $\alpha(r)$ and $N_e(r)$, together with the inferred curves $A_{\text{fit}}(x)$ obtained from the forward process of Section V, for the four snapshot times. In each case, we set $W_i = 0.05$ in eq. (30) within windows estimated to be broad enough to exclude refraction effects (700-820 μm , 590-730 μm , 480-620 μm , and 370-500 μm , respectively). Figs. 15(e)-15(h) show comparisons between the actual $\alpha(r)$ and $N_e(r)$ profiles, and the inferred profiles $\alpha_{\text{fit}}(r)$ and $N_{\text{efit}}(r)$ obtained from the forward and backward processing of Section IV and V. We see that in general the agreement is very good throughout the 19.3 - 20.8 ns time history, including at later times

when $\alpha(r)$ develops a significant non-Gaussian tail due to the opacity of the ablated shell material.

We can quantify the accuracy obtained by selecting a number of metrics defining the $\alpha(r)$ and $N_e(r)$ profiles. The $\alpha(r)$ and $N_e(r)$ profile widths (defined here to be the separation between the outer peaks of $d^2N_e(r)/dr^2$) are measures of inflight compression of the shell and shell-plus-ice masses, respectively, with the latter width being larger and not measureable at these times by absorption radiography due to the low x-ray opacity of the ice. The radii at peak α or N_e are important for implosion velocity measurements. We also examine the peak value of N_e and the integral of $\alpha(r)r^2dr$ within the windows shown in Figs. 15(e)-15(h); the latter quantity would be expected to be proportional to the remaining mass of the shell, which is an important implosion performance metric [3].

The results are tabulated in Table I along with the errors in the inferred quantities vs. the actual quantities. We see that the widths and radii are correctly inferred within approximately 10 μm and 5 μm , respectively, comparable to the spatial resolution of the measurements, and that both peak N_e and $\int \alpha(r)r^2dr$ are correctly inferred within 5 - 10%. The inferred $N_e(r)$ profile widths are generally wider than the actual widths, largely due to uncorrected blurring but partly due to the gradient term in eq. (14) that is neglected in the back-analysis procedure of Section IV. However, empirically reducing the measured widths by an amount equal to the effective object spatial resolution brings the widths into agreement well within the $\sim 7 - 12 \mu\text{m}$ resolution element of the data. We note that the excellent agreement in peak N_e may be fortuitous given the results shown in Section IV using unblurred radiograph profiles (Fig. 9). The main effects of uncorrected blurring of the refraction-enhanced radiographs appears to be a reduction of the inferred

peak N_e and a broadening of the inferred $N_e(r)$ profile. The former effect is actually helpful, and the second effect can be approximately corrected empirically.

These results are typical of other low-opacity capsule simulations we have examined, including pathological cases where drive temporal variations or catastrophic instability-driven mix cause dramatic changes in the shape of the observed refraction-enhanced image data and in the inferred profile widths. For illustrative purposes, we show one such comparison in Figure 16. Fig. 16(a) shows a time sequence of simulated refraction-enhanced radiographs from the nominal simulation analyzed earlier in this section, and Fig. 16(b) shows a sequence of simulated refraction-enhanced radiographs taken at the same times from a pathological simulation of the same capsule driven by a temporally fluctuating drive. Marked differences are evident in the radiograph data, particularly early in time, that would be obvious even to the eye, and the radiographs can be analyzed as described here to infer markedly different radial profiles, particularly showing different widths and structure in the $N_e(r)$ curve that are not be observable in absorption radiograph data.

VII. Summary

We have shown that point-projection x-ray radiographs of implosion plasmas relevant to ICF experiments at the NIF will show significant refraction features at relevant x-ray energies and backlight distances (10 keV, 10 mm), resulting in refraction-enhanced radiograph profiles $T(x)$ that differ qualitatively and quantitatively from absorption radiograph profiles $A(x)$ obtained with pinhole imagers and area backlights. Peaks and dips in $T(x)$ can be understood in terms of derivatives of the total electron areal

density $\rho(x)$ through the limb of the implosion, enabling inference of the total electron radial density profile $N_e(r)$ even through regions of the plasma that do not significantly absorb the backlight x-rays, including through plasma formed from initially cryogenic hydrogen ice. We have used geometrical optics to develop an equation, eq. (14), that is essentially an exact solution to the Fresnel-Kirchoff integral in the geometrical optics limit [23] and describes $T(x)$ in terms of both $\rho(x)$ and the optical depth profile $\tau(x)$, and we have explored limits where these terms are separable in eq. (10), allowing separate analysis to determine both $N_e(r)$ and the absorption radial profile $\alpha(r)$.

We have used these analytical results to develop analytical and numerical data analysis procedures to extract approximate $\alpha(r)$ and $N_e(r)$ from refraction-enhanced radiographs of implosion plasmas. $\alpha(r)$ is determined using a model profile that allows the possibility of a significant tail extending to large radius, as is expected based on implosion hydrodynamics simulations, and we extract a best-fit model $\alpha_{\text{fit}}(r)$ by fitting in radiograph space including spatial blurring, second-order backlight non-uniformities, and data noise. Using the measured $T(x)$ and the best-fit $A_{\text{fit}}(x)$, we can then determine an approximate $N_{\text{efit}}(r)$ through a backwards inversion process based on eq. (10). We have shown that this data analysis procedure returns good approximations to $\alpha(r)$ and $N_e(r)$, and we have quantified the accuracy expected for realistic implosion plasma profiles, using a realistic backlight size (5 μm) and temporal resolution (40 ps).

Measurement of $N_e(r)$ (width, peak and peak radius, radial structure) would be a new capability in implosion plasma diagnosis, and measurement of $\alpha(r)$ from the same plasma using the same data allows comparison between the two profiles that would isolate the thickness of the hydrogen plasma surrounded by the opaque shell plasma in

cryogenic layered implosions. Finally, the uniform nature of illumination by a point-like backlight eliminates significant source of error in the interpretation of pinhole-imaging absorption radiographs in current experiments, likely allowing for more accurate measurements of important parameters like remaining mass. We expect to implement this implosion diagnostic capability in the near future, and the experimental results will be reported elsewhere.

In situations where eq. (10) is a poor approximation to eq. (14) (large f , λ or $d\rho/dx$, particularly when τ is large), then the inversion process described in Section IV breaks down, the approximation $T(x) = A(x)R(x)$ implicit in Section V no longer holds, and the only recourse is to use a simultaneous forward-model fit procedure to both $\alpha(r)$ and $N_e(r)$ using eq. (14), possibly starting with the results of Sections IV and V as initial trial functions. When this becomes necessary, it may be advantageous to define $\alpha(r)$ and $N_e(r)$ on a radial grid, rather than assume they follow analytical model functions, and vary the abscissa and ordinate points utilizing genetic-algorithm search procedures similar to those developed for use in x-ray spectroscopy data analysis [29] and currently being explored for use in NIF absorption radiography data analysis. This capability would be particularly valuable for analysis of refraction-enhanced radiography data very early in the implosion, when density gradients are steep and when shocks are transiting the shell and ice layers. This could allow an independent measure of shock timing that currently can only be diagnosed in surrogate targets [25], requiring reliance on simulations to verify the surrogacy with actual implosion targets.

When refraction dominates absorption but is still very weak (e.g. at much higher x-ray backlight energy), other techniques could be utilized to infer $\rho(x)$ and therefore

$N_e(r)$. Phase-contrast imaging using diffraction gratings has been proposed [17] for laser-produced plasma diagnosis, and the utility of this approach for diagnosing implosion plasmas would be clarified by refraction-enhanced radiography data of the type described here. Other plausible approaches capable of diagnosing small refractive effects include crystal analyzers [30], Moiré deflectometry [31], and Hartmann sensors [32]. These will all be limited ultimately by available x-ray backlight brightness at higher x-ray energies, so inclusion of realistic capabilities in the experiment planning process is critical in evaluating the viability of phase-sensitive techniques at multi-tens-of-keV x-ray energies. Additionally, short-pulse laser-produced backlights could become necessary due to their relatively high conversion efficiency at high x-ray energies [33]; such backlights have already been utilized for high-energy implosion radiography experiments at the Omega Laser Facility [34], and are planned for the NIF.

Throughout we have used the standard ionized-plasma form of the index of refraction, $n = 1 - r_e \lambda^2 N_e / 2\pi$. However, when n is calculated by more sophisticated means we can use it directly, in which case eq. (14) becomes,

$$T\left(x + f \frac{d\eta}{dx}\right) = \frac{e^{-\tau(x)}}{\left|1 + f \frac{d^2\eta}{dx^2}\right|} \quad (31)$$

and eq. (10) becomes,

$$T(x) = e^{-\tau(x)} \left(1 - f \frac{d^2\eta}{dx^2}\right) \quad (32)$$

where η is the Abel transform of $(n(r)-1)$,

$$\eta(x) = 2 \int_x^\infty \frac{r(n(r)-1)dr}{\sqrt{r^2 - x^2}} \quad (33)$$

Since $(n-1)$ changes sign depending on whether n is greater than unity or less than unity, this implies that across a spectral region near a resonance where the plasma index of refraction becomes greater than unity [35-37], the refraction-enhanced radiograph pattern will change significantly, with peaks and dips inverting and with shifts in eq. (31) changing sign. This is analogous to plasma interferometry measurements, where fringes bend in unexpected directions because of the contributions of bound electrons to the index of refraction in certain x-ray energy regimes [36]. Similar anomalous dispersion effects have been observed with high-energy gamma-rays for different physical reasons [38]. Relatively simple refraction-enhanced backlighting of suitable plasmas in suitable x-ray energy regimes could probe refractive index variations using conventional backlights, possibly coupled to a spectrometer to disperse the backlight x-rays in a direction perpendicular to a one-dimensional space axis. Eq. (31) generalizes readily to non-spherically-symmetric plasmas through a modification of eq. (33), and the data analysis process described here can be readily modified for other kinds of symmetry.

We thank M. Barrios, P. Di Nicola, K. Fournier, D. Hicks, J. Lugten, R. Olson, K. Opachich, R. Wallace, and the operations and target diagnostics staff at Omega and the NIF for their contributions and support. This work was performed under the auspices of the U.S. Department of Energy by Lawrence Livermore National Laboratory under contract DE-AC52-07NA27344.

References

1. D. H. Kalantar, S. W. Haan, B. A. Hammel, C. J. Keane, O. L. Landen, and D. H. Munro, "X-ray backlit imaging measurement of in-flight pusher density for an indirect drive capsule implosion", *Rev. Sci. Instrum.* **68**, 814-816 (1997).
2. F. J. Marshall, P. W. McKenty, J. A. Delettrez, R. Epstein, J. P. Knauer, V. A. Smalyuk, J. A. Frenje, C. K. Li, R. D. Petrasso, F. H. Sequin, and R. C. Mancini, "Plasma-density determination from x-ray radiography of laser-driven spherical implosions", *Phys. Rev. Lett.* **102**, 185004 (2009).
3. D. G. Hicks, B. K. Spears, D. G. Braun, R. E. Olson, C. M. Source, P. M. Celliers, G. W. Collins, and O. L. Landen, "Convergent ablator performance measurements", *Phys. Plasmas* **17**, 102703 (2010).
4. R. E. Olson, D. G. Hicks, N. B. Meezan, J. A. Koch, and O. L. Landen, "Comparisons of NIF convergent ablator simulations with radiograph data", *Rev. Sci. Instrum.* **83**, 10D310 (2012).
5. J. A. Koch, N. Izumi, L. A. Welser, R. C. Mancini, S. W. Haan, T. W. Barbee, Jr., S. Dalhed, I. E. Golovkin, L. Klein, R. W. Lee, F. J. Marshall, D. Meyerhofer, H. Nishimura, Y. Ochi, T. C. Sangster, and V. Smalyuk, "Core temperature and density profile measurements in inertial confinement fusion implosions", *High Energy Density Physics* **4**, 1-17 (2008).
6. B. J. Kozioziemski, J. A. Koch, A. Barty, H. E. Martz, Jr., W-K. Lee, and K. Fezzaa, "Quantitative characterization of inertial confinement fusion capsules using phase contrast enhanced x-ray imaging", *J. Appl. Phys.* **97**, 063103 (2005).

7. J. A. Koch, O. L. Landen, B. J. Kozioziemski, N. Izumi, E. L. Dewald, J. D. Salmonson, and B. A. Hammel, "Refraction-enhanced x-ray radiography for inertial confinement fusion and laser-produced plasma applications", *J. Appl. Phys.* **105**, 113112 (2009).
8. J. Workman, J. Cobble, K. Flippo, D. C. Gautier, D. S. Montgomery, and D. T. Offerman, "Phase contrast imaging using ultrafast x-rays in laser-shocked materials", *Rev. Sci. Instrum.* **81**, 10E520 (2010).
9. Y. Ping, O. L. Landen, D. G. Hicks, J. A. Koch, R. Wallace, C. Sorce, B. A. Hammel, and G. W. Collins, "Refraction-enhanced x-ray radiography for density profile measurements at CH/Be interface", *J. Instrum.* **6**, P09004 (2011).
10. D. Chapman, W. Thomlinson, R. E. Johnson, D. Washburn, E. Pisano, N. Gmür, Z. Zhong, R. Menk, F. Arfelli, and D. Sayers, "Diffraction enhanced x-ray imaging", *Phys. Med. Biol.* **42**, 2015-2025 (1997).
11. N. Yagi, Y. Suzuki, K. Umetani, Y. Kohmura, and K. Yamasaki, "Refraction-enhanced x-ray imaging of mouse lung using synchrotron radiation source", *Med. Phys.* **26**, 2190-2193 (1999).
12. J. Keyriläinen, M. Fernández, and P. Suortti, "Refraction contrast in x-ray imaging", *Nuc. Instrum. Meth. Phys. Res. A* **488**, 419-427 (2002).
13. M. N. Wernick, Y. Yang, I. Mondal, D. Chapman, M. Hasnah, C. Parham, E. Pisano, and Z. Zhong, "Computation of mass-density images from x-ray refraction-angle images", *Phys. Med. Biol.* **51**, 1769-1778 (2006).
14. A. Clegg, A. L. Fey, and T. J. W. Lazio, "The gaussian plasma lens in astrophysics: Refraction", *Astrophys. J.* **496**, 253-266 (1998).

15. J. A. Koch, O. L. Landen, T. W. Barbee, Jr., P. Celliers, L. B. Da Silva, S. G. Glendinning, B. A. Hammel, D. H. Kalantar, C. Brown, J. Seely, G. R. Bennett, and W. Hsing, "High-energy x-ray microscopy techniques for laser-fusion plasma research at the National Ignition Facility", *Appl. Opt.* **37**, 1784-1795 (1998).
16. A. Pogany, D. Gao, and S. W. Wilkins, "Contrast and resolution in imaging with a microfocus x-ray source", *Rev. Sci. Instrum.* **68**, 2774-2782 (1997).
17. D. Stutman and M. Finkenthal, "Talbot-Lau x-ray interferometry for high energy density plasma diagnostic", *Rev. Sci. Instrum.* **82**, 113508 (2011).
18. X. Wu and H. Liu, "A general theoretical formalism for x-ray phase contrast imaging", *J. X-ray Science and Technology* **11**, 33-42 (2003).
19. T. E. Gureyev and S. W. Wilkins, "On x-ray phase imaging with a point source", *J. Opt. Soc. Am. A* **15**, 579-585 (1998).
20. J. A. Koch, J. D. Sater, A. J. MacKinnon, T. P. Bernat, D. N. Bittner, G. W. Collins, B. A. Hammel, E. R. Mapoles, and C. H. Still, "Numerical raytrace verification of optical diagnostics of ice surface roughness for inertial confinement fusion experiments", *Fusion Sci. and Tech.* **43**, 55-66 (2003).
21. S. H. Glenzer, D. A. Callahan, A. J. Mackinnon, J. L. Kline *et al.*, "Cryogenic thermonuclear fuel implosions on the National Ignition Facility", *Phys. Plasmas* **19**, 056318 (2012).
22. The forward and backward Abel transform integrals can be solved exactly when the transform function $f(r)$ or $dF(x)/dx$ is described by discrete points connected by straight lines, and assumed to be zero outside bounds $[a,b]$. This numerical approach is utilized throughout.

23. J. A. Koch, O. L. Landen, L. J. Suter, and L. P. Masse, "A simple solution to the Fresnel-Kirchoff diffraction integral for application to refraction-enhanced radiography", manuscript in preparation.
24. D. S. Clark, S. W. Haan, A. W. Cook, M. J. Edwards, B. A. Hammel, J. M. Koning, and M. M. Marinak, "Short wavelength and three-dimensional instability evolution in National Ignition Facility ignition capsule designs", *Phys. Plasmas* **18**, 082701 (2011).
25. H. F. Robey, P. M. Celliers, J. L. Kline, A. J. Mackinnon *et al.*, "Assembly of high-areal-density deuterium-tritium fuel from indirectly driven cryogenic implosions", *Phys. Rev. Lett.* **108**, 215004 (2012).
26. Y. Suzuki, N. Yagi, and K. Uesugi, "X-ray refraction-enhanced imaging and a method for phase retrieval for a simple object", *J. Synchrotron Rad.* **9**, 160-165 (2002).
27. A. B. Bullock, O. L. Landen, B. E. Blue, J. Edwards, and D. K. Bradley, "X-ray induced pinhole closure in point-projection x-ray radiography", *J. Appl. Phys.* **100**, 043301 (2006).
28. M. Marinak, S. W. Haan, T. R. Dittrich, R. E. Tipton, and G. B. Zimmerman, "A comparison of three-dimensional multimode hydrodynamic growth on various National Ignition Facility capsule designs with HYDRA simulations", *Phys. Plasmas* **5**, 1125-1132 (1998).
29. I. Golovkin, R. Mancini, S. Louis, Y. Ochi, K. Fujita, H. Nishimura, H. Shirga, N. Miyanaga, H. Azechi, R. Butzback, I. Uschmann, E. Förster, J. Delettrez, J. Koch, R. W. Lee, and L. Klein, "Spectroscopy determination of dynamic plasma gradients in implosion cores", *Phys. Rev. Lett.* **88**, 045002 (2002).

30. E. Förster, K. Goetz, and P. Zaumseil, "Double crystal diffractometry for the characterization of targets for laser fusion experiments", *Kristall und Technik* **15**, 937-945 (1980).
31. J. Ruiz-Camacho, F. N. Beg, and P. Lee, "Comparison of sensitivities of Moire deflectometry and interferometry to measure electron densities in z-pinch plasmas", *J. Phys. D.* **40**, 2026-2032 (2007).
32. K. Baker, J. Brase, M. Kartz, S. S. Olivier, B. Sawvel, and J. Tucker, "Electron density characterization by use of a broadband x-ray-compatible wave-front sensor", *Opt. Lett.* **28**, 149-151 (2003).
33. H. S. Park, N. Izumi, M. H. Key, J. A. King, J. A. Koch, O. L. Landen, P. K. Patel, D. F. Price, B. A. Remington, H. F. Robey, R. A. Snavely, M. Tabak, R. P. J. Town, J. E. Wickersham, C. Stoeckl, M. Storm, W. Theobald, D. M. Chambers, R. Eagleton, T. Goldsack, R. J. Clarke, R. Heathcote, E. Giraldez, A. Nikroo, D. A. Steinman, R. B. Stephens, and B. B. Zhang, "High-energy K-alpha radiography using high-intensity, short-pulse lasers", *Phys. Plasmas* **13**, 056309 (2006).
34. R. Tommasini, S. P. Hatchett, D. S. Hey, C. Iglesias, N. Izumi, J. A. Koch, O. L. Landen, A. J. MacKinnon, C. Sorce, J. A. Delettrez, V. Y. Glebov, T. C. Sangster, and C. Stoeckl, "Development of compton radiography of inertial confinement fusion implosions", *Phys. Plasmas* **18**, 056309 (2011).
35. J. Nilsen and J. H. Scofield, "Plasmas with an index of refraction greater than 1", *Opt. Lett.* **29**, 2677-2679 (2004).
36. J. Filevich, J. J. Rocca, M. C. Marconi, S. J. Moon, J. Nilsen, J. H. Scofield, J. Dunn, R.F. Smith, R. Keenan, J. R. Hunter, and V. N. Shlyaptsev, "Observation of multiply

ionized plasma with index of refraction greater than one", Phys. Rev. Lett. **94**, 035005 (2005).

- 37. J. Nilsen and W. R. Johnson, "Plasma interferometry and how the bound-electron contribution can bend fringes in unexpected ways", Appl. Opt. **44**, 7295-7301 (2005).
- 38. D. Habs, M. M. Günther, M. Jentschel, and W. Urban, "Refractive index of silicon at γ ray energies", Phys. Rev. Lett. **108**, 184802 (2012).

Figure Captions

Figure 1: Geometry of backlit imaging with a point-like backlight (a) and with a pinhole and an area backlight (b). In both cases, the visibility of refraction effects that tend to steer the curved ray depend on the size of the backlight.

Figure 2: $N_e(r)$ and $\alpha(r)$ profiles derived from implosion hydrodynamics simulation output, smoothed with a Gaussian blur with a 5 μm FWHM (a), and simulated absorption and total (refraction and absorption) radiograph profiles from a 10 keV point-backlight at a distance of 10 mm from the center of the implosion plasma, calculated both by raytracing and by eq. (10) (b). No spatial blurring of the radiographs is applied, and the noise in the raytrace radiograph is statistical noise due to a finite number of randomly-directed rays.

Figure 3: $N_e(r)$ and $\alpha(r)$ profiles derived from implosion hydrodynamics simulation output, smoothed with a Gaussian blur with a 1 μm FWHM (a), and simulated absorption and total (refraction and absorption) radiograph profiles from a 10 keV point-backlight at a distance of 10 mm from the center of the implosion plasma, calculated both by raytracing and by eq. (10) (b). No spatial blurring of the radiographs is applied, and the noise in the raytrace radiograph is statistical noise due to a finite number of randomly-directed rays.

Figure 4: Sketch showing the geometry of a ray incident from above that is refracted by an absorbing and phase-shifting object with an incident surface profile described by $s(x)$.

Figure 5: Simulated total (refraction and absorption) radiograph profiles from a 10 keV point-backlight at a distance of 10 mm from the center of the implosion plasma, using the $N_e(r)$ and $\alpha(r)$ profiles from Fig. 2(a) (a) and using the $N_e(r)$ and $\alpha(r)$ profiles from Fig. 3(a) (b), calculated both by raytracing and by eq. (14). No spatial blurring of the

radiographs is applied, and the noise in the raytrace radiograph is statistical noise due to a finite number of randomly-directed rays.

Figure 6: Simulated total (refraction and absorption) radiograph profiles from a 10 keV point-backlight at a distance of 10 mm from the center of the implosion plasma, using the $N_e(r)$ and $\alpha(r)$ profiles from Fig. 2(a) (a) and using the $N_e(r)$ and $\alpha(r)$ profiles from Fig. 3(a) (b), calculated both by numerical Fresnel-Kirchoff diffraction integrals and by eq. (14). No spatial blurring of the radiographs is applied.

Figure 7: $N_e(r)$ profile from Fig. 2(a), compared with a $N_{\text{fit}}(r)$ profile inferred from the refraction part of the raytrace radiograph in Fig. 2(b) using eqs. (22-25), with a data window from 350-700 μm .

Figure 8: Refraction $R(x)$ and total/absorption $T(x)/A(x)$ radiograph profiles from the $N_e(r)$ and $\alpha(r)$ profiles from Fig. 2(a), calculated by eq. (14). No spatial blurring of the radiographs is applied.

Figure 9: $N_e(r)$ profile from Fig. 2(a), compared with a $N_{\text{fit}}(r)$ profile inferred from the $T(x)/A(x)$ curve of Fig. 7 using eqs. (22-25), with a data window from 350-700 μm .

Figure 10: Analytical $\alpha(r)$ profile using eq. (28) with $C = 0.004 \mu\text{m}^{-1}$, $D = 10 \mu\text{m}$, $r_0 = 482 \mu\text{m}$, and $\gamma = 0.9$, and calculated unblurred radiograph profile $A(x)$ (solid lines), together with a best fit to the radiograph profile $A_{\text{fit}}(x)$ using eq. (30) and the corresponding fit $\alpha_{\text{fit}}(r)$ profile (dashed lines).

Figure 11: Analytical $\alpha(r)$ profile using eq. (28) with $C = 0.004 \mu\text{m}^{-1}$, $D = 10 \mu\text{m}$, $r_0 = 482 \mu\text{m}$, and $\gamma = 0.9$, and calculated radiograph profile $A(x)$ blurred with a 20 μm FWHM-Gaussian function (solid lines), together with a best fit to the radiograph profile $A_{\text{fit}}(x)$ using eq. (30) and the corresponding fit $\alpha_{\text{fit}}(r)$ profile (dashed lines).

Figure 12: Analytical $\alpha(r)$ profile using eq. (28) with $C = 0.004 \mu\text{m}^{-1}$, $D = 10 \mu\text{m}$, $r_0 = 482 \mu\text{m}$, and $\gamma = 0.9$, and calculated radiograph profile $A(x)$ blurred with a $20 \mu\text{m}$ FWHM-Gaussian function, offset with a non-uniform backlight profile ($D = 0.0875$, $E = -7.5 \times 10^{-5}$, $F = -2.5 \times 10^{-7}$ in eq. (27)), and randomly noised with a standard deviation of 0.03 per $0.1\text{-}\mu\text{m}$ pixel (solid lines), together with a best fit to the radiograph profile $A_{\text{fit}}(x)$ using eq. (30) and the corresponding fit $\alpha_{\text{fit}}(r)$ profile (dashed lines).

Figure 13: $\alpha(r)$ profile from Fig. 2(a) and calculated absorption radiograph $A(x)$ (solid lines), together with a best fit to the radiograph profile using eq. (30) and the corresponding fit $\alpha(r)$ profile (dashed lines). Optimum fit parameters in eq. (28) are $C = 0.0041 \mu\text{m}^{-1}$, $D = 8.4 \mu\text{m}$, $r_0 = 481.5 \mu\text{m}$, and $\gamma = 0.89$.

Figure 14: $\alpha(r)$ profile and calculated refraction-enhanced radiograph from Fig. 2(a) (solid lines), together with a best fit to the radiograph profile $A_{\text{fit}}(x)$ using eq. (30) and the corresponding fit $\alpha_{\text{fit}}(r)$ profile (dashed lines). Here, the radiograph points within the bounds $x = 435$ and $520 \mu\text{m}$ were de-weighted by a factor of 0.05 compared with the radiograph points outside these bounds. Optimum fit parameters in eq. (28) are $C = 0.0038 \mu\text{m}^{-1}$, $D = 9.4 \mu\text{m}$, $r_0 = 481.6 \mu\text{m}$, and $\gamma = 0.82$.

Figure 15: Synthetic absorption $A(x)$ and refraction-enhanced $T(x)$ radiographs, processed as described in Section VI, along with forward-fit $A_{\text{fit}}(x)$ profiles derived from $T(x)$, at four different times in the simulation; 19.3 ns (a), 19.9 ns (b), 20.4 ns (c), and 20.8 ns (d). Simulated $\alpha(r)$ and $N_e(r)$ curves at the same times are shown in (e), (f), (g) and (h) respectively, along with the inferred curves $\alpha_{\text{fit}}(r)$ and $N_{\text{efit}}(r)$ derived from the $T(x)$ radiographs.

Figure 16: Synthetic gray-scale refraction-enhanced radiographs at times 19.3, 19.6, 19.9, 20.2, 20.4, 20.6 and 20.8 ns, for a nominal simulation (a) and for a pathological simulation (b) of the same capsule driven by a temporally fluctuating drive that launches additional shocks into the implosion.

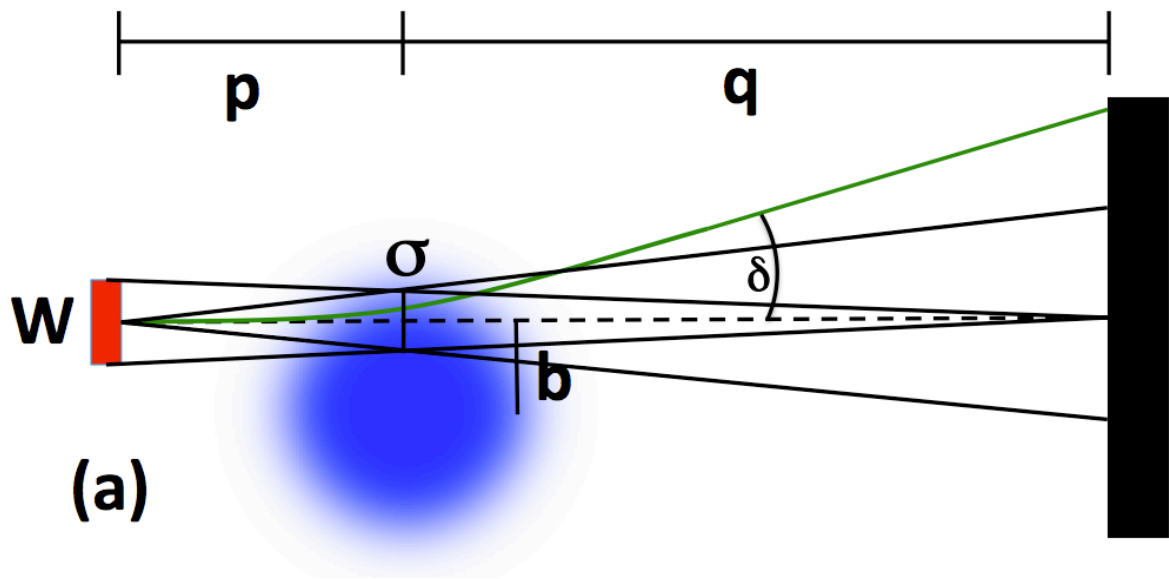


Figure 1(a)

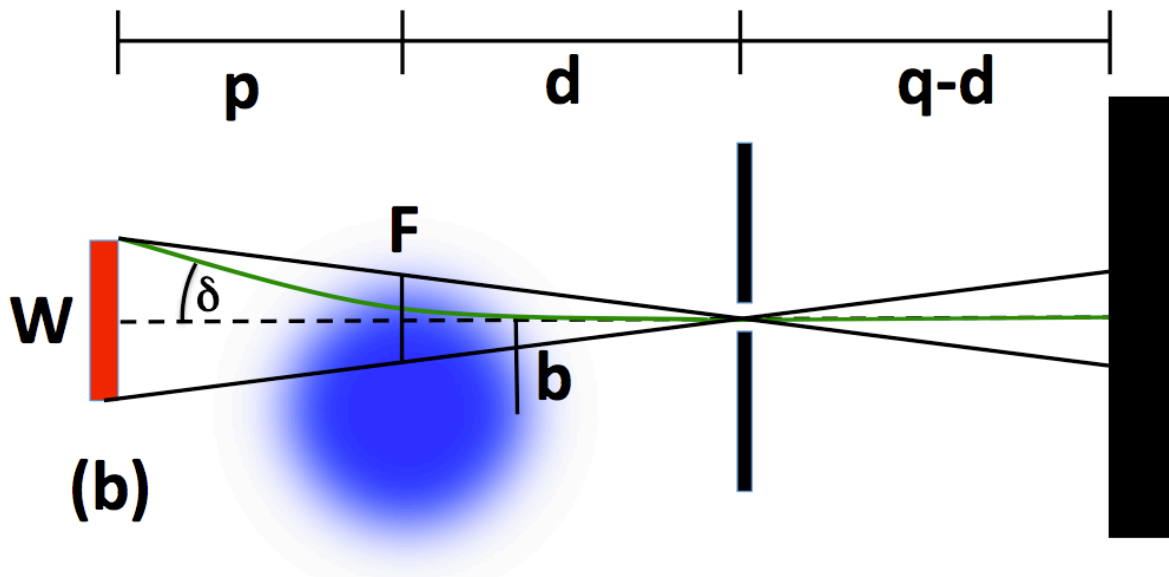


Figure 1(b)

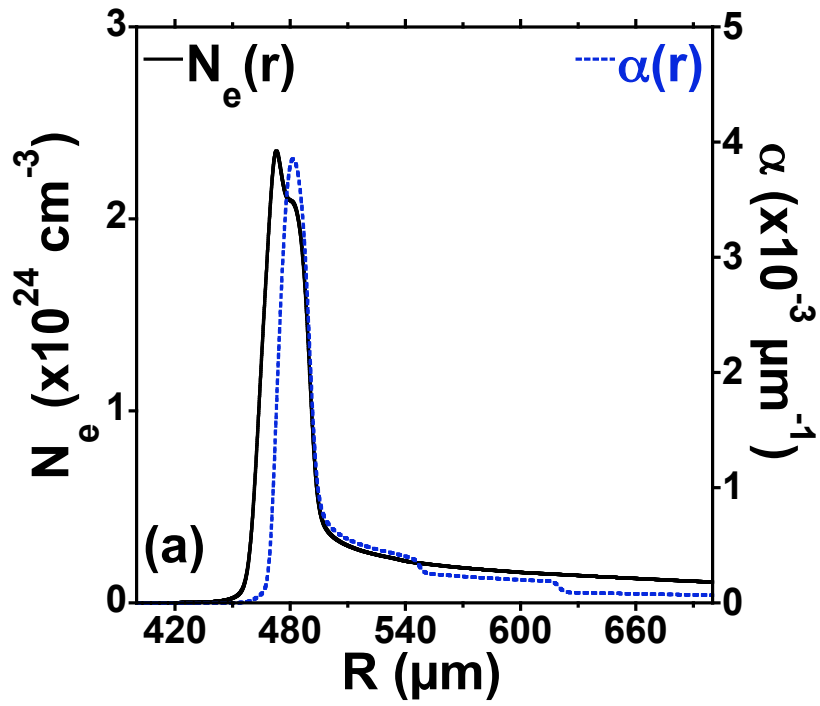


Figure 2(a)

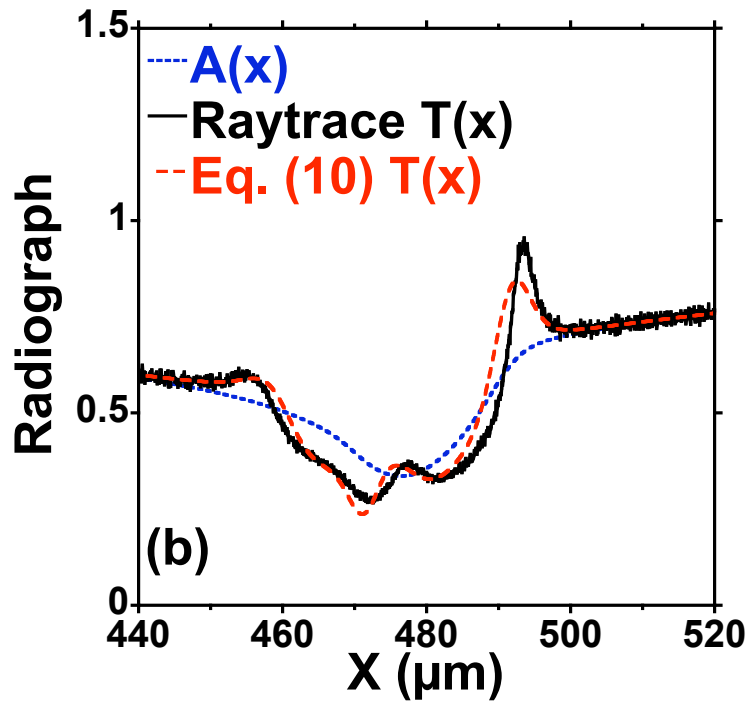


Figure 2(b)

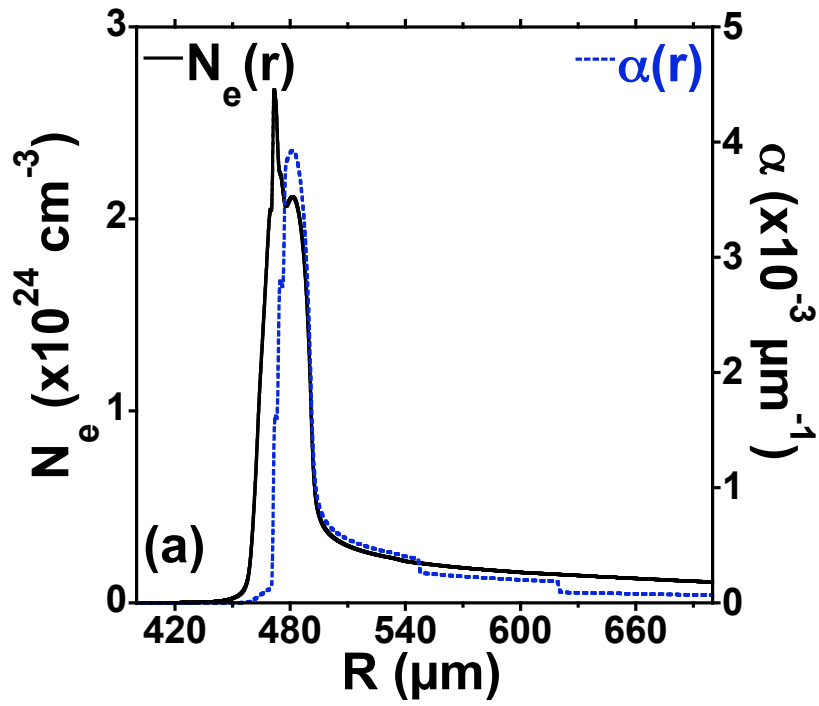


Figure 3(a)

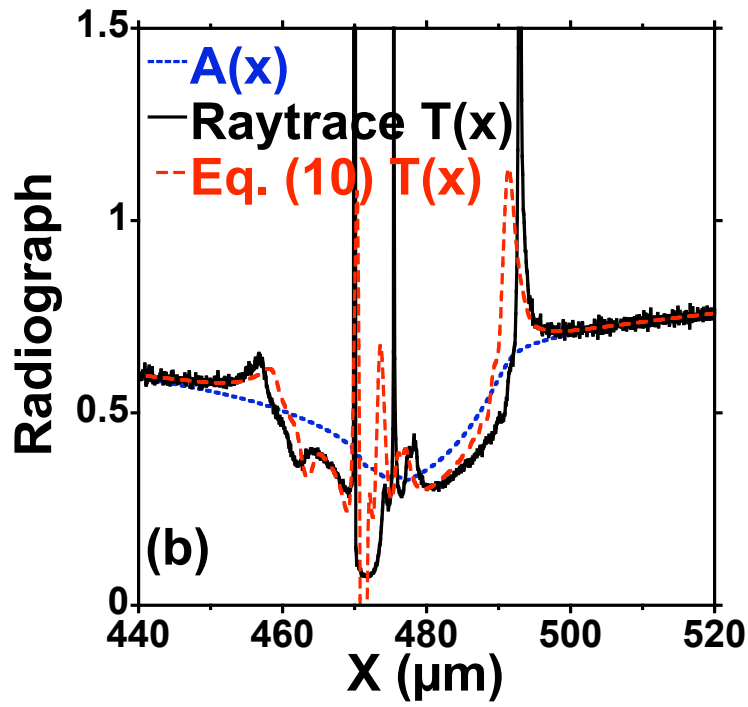


Figure 3(b)

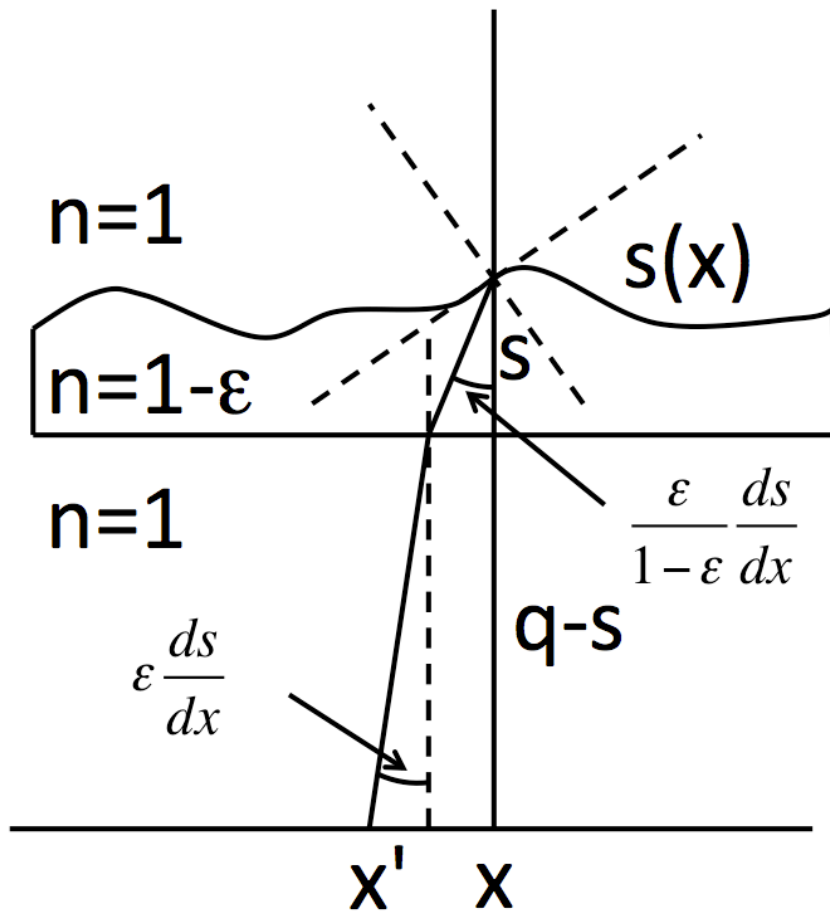


Figure 4

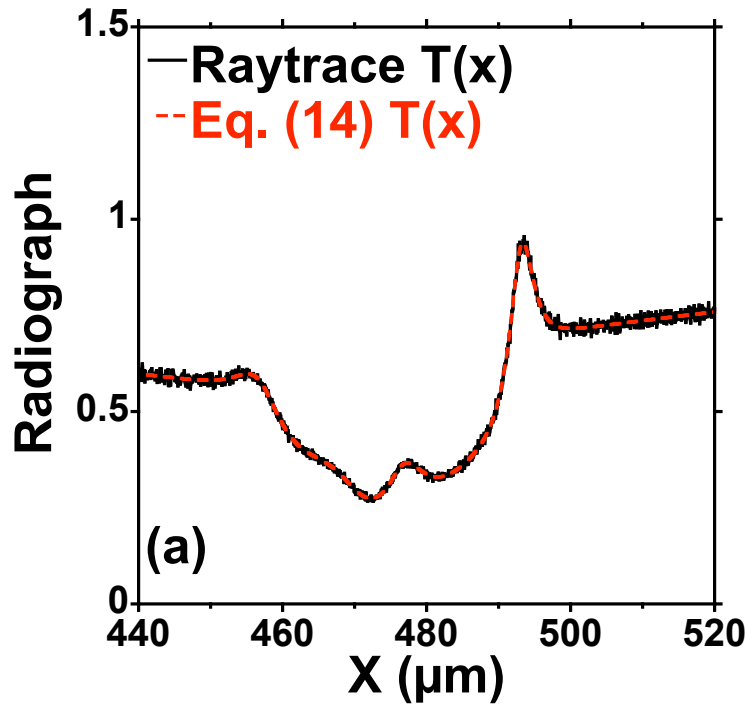


Figure 5(a)

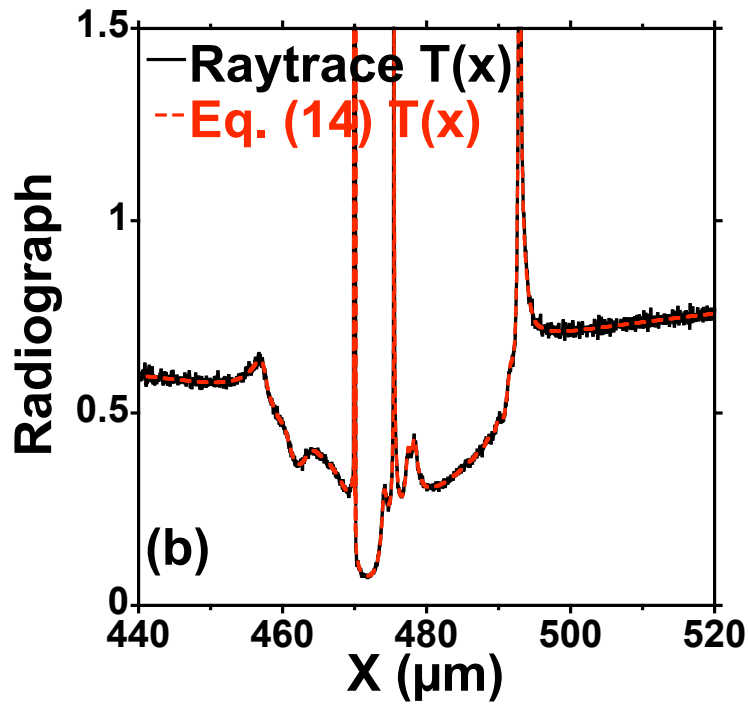


Figure 5(b)

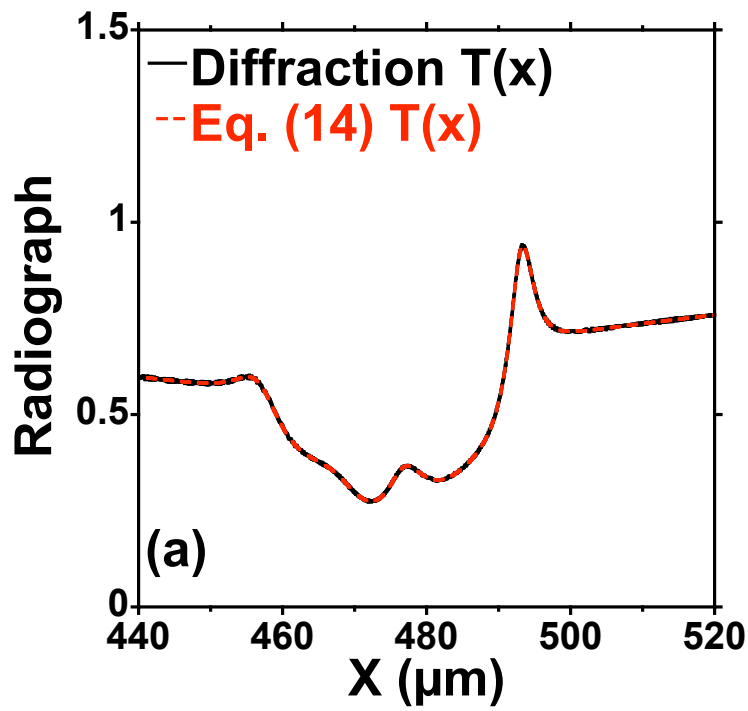


Figure 6(a)

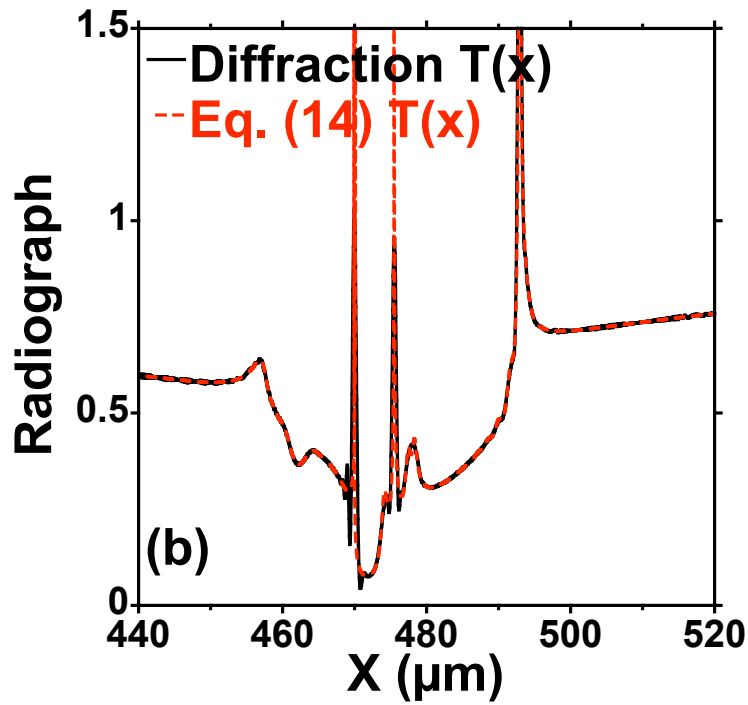


Figure 6(b)

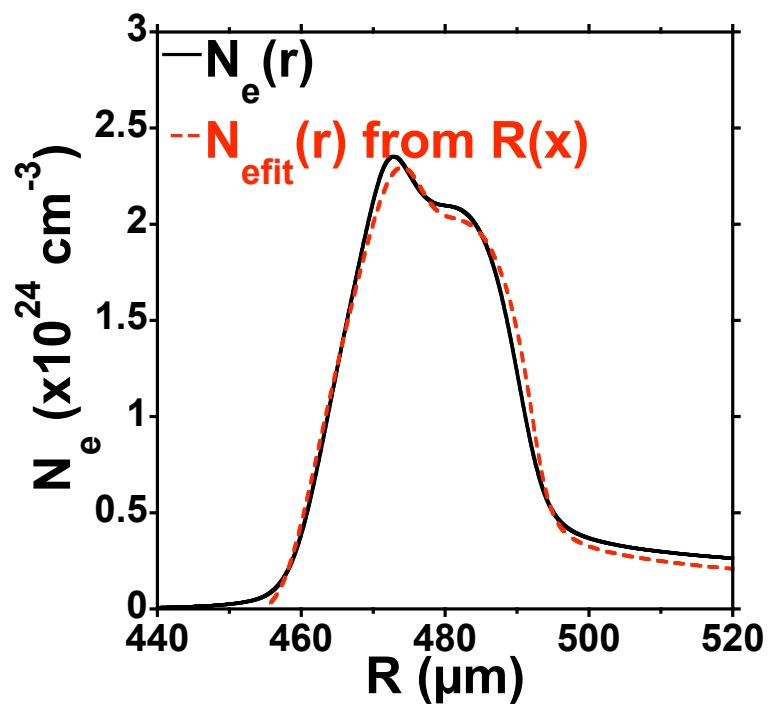


Figure 7

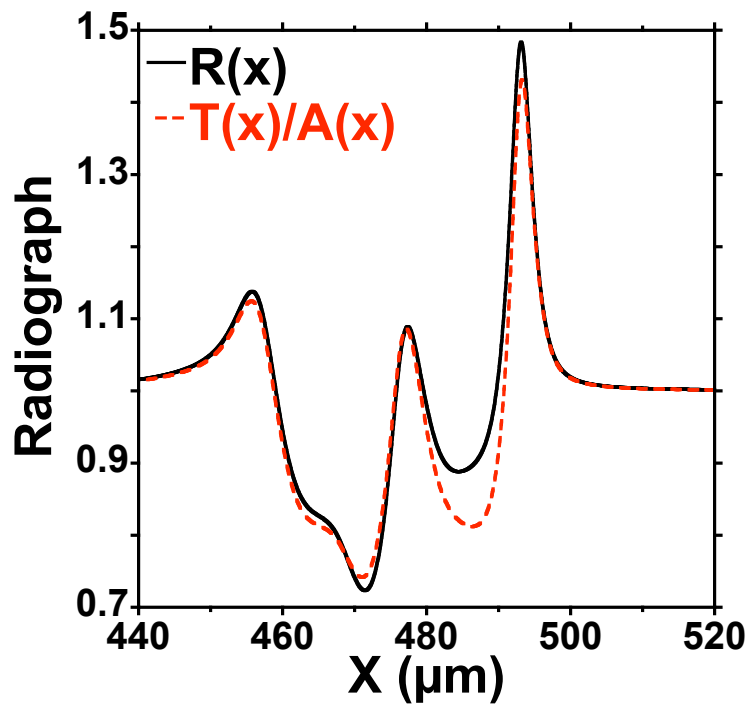


Figure 8

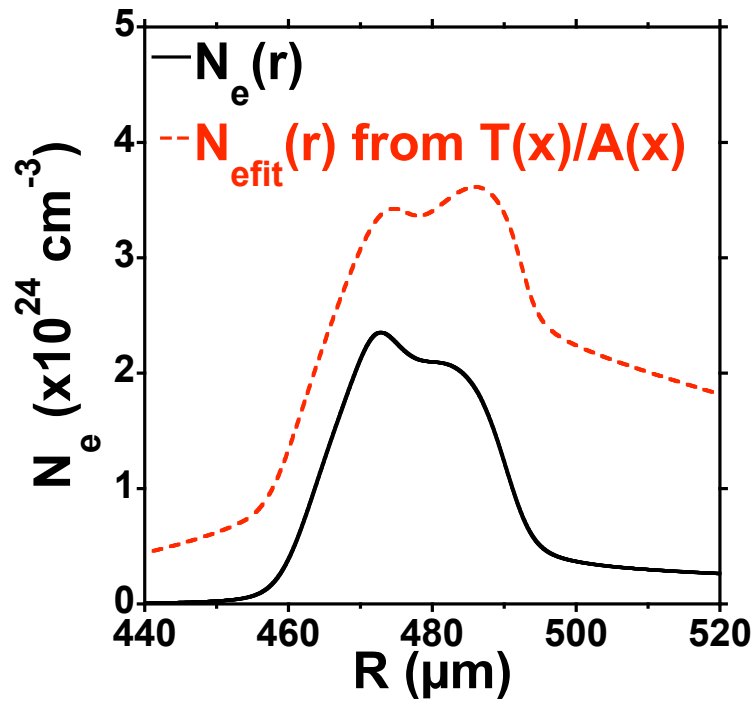


Figure 9

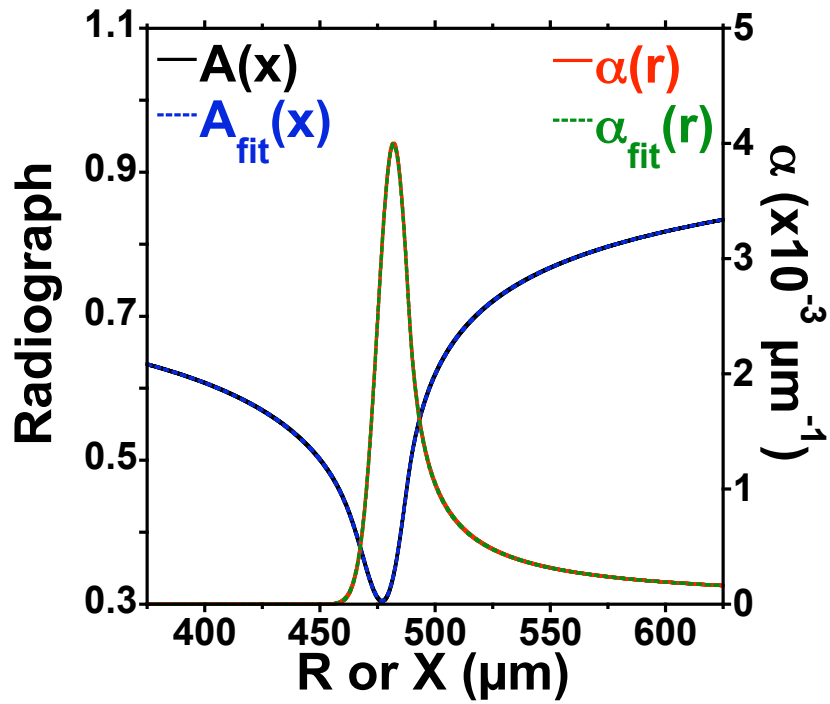


Figure 10

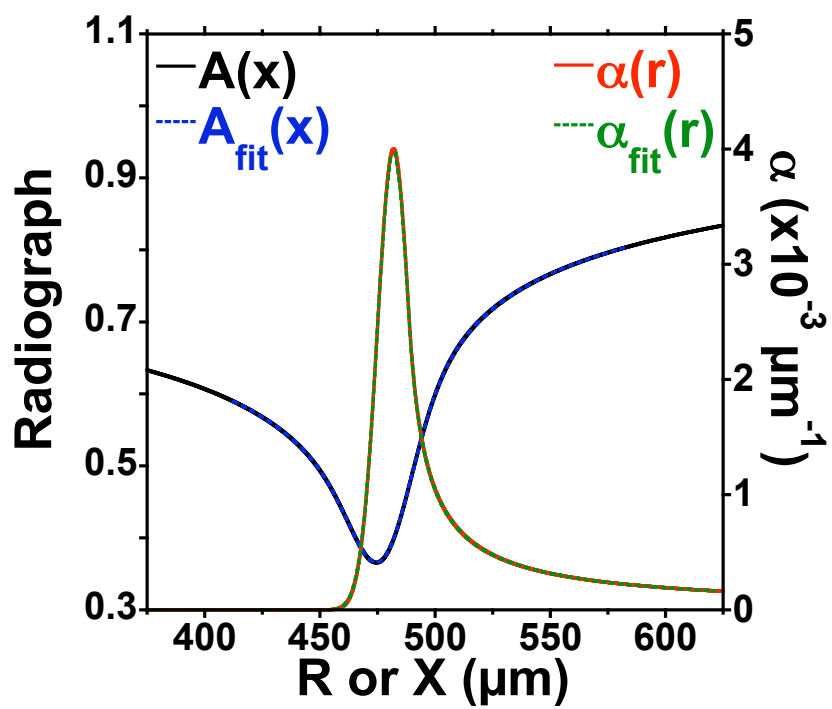


Figure 11

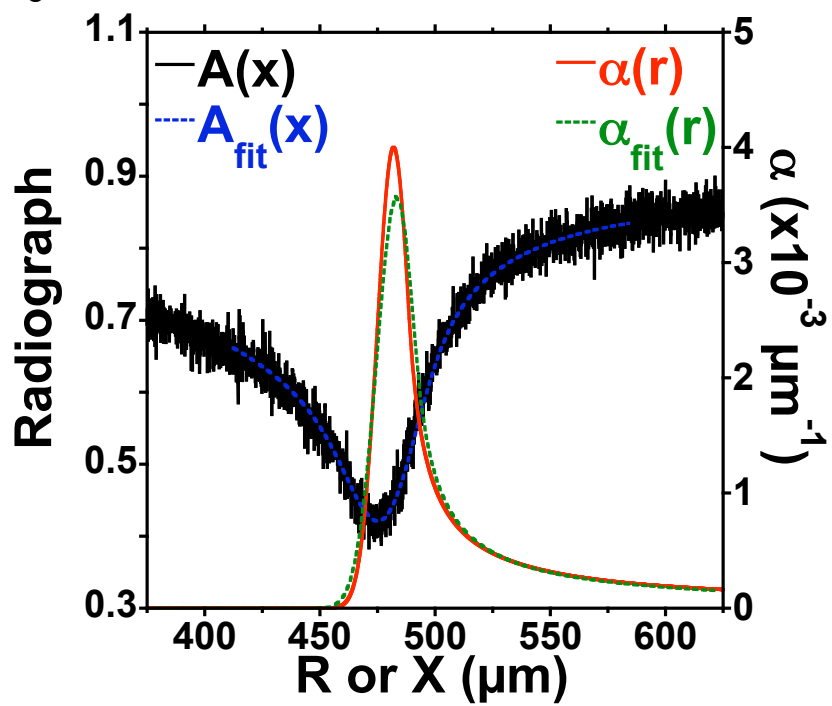


Figure 12

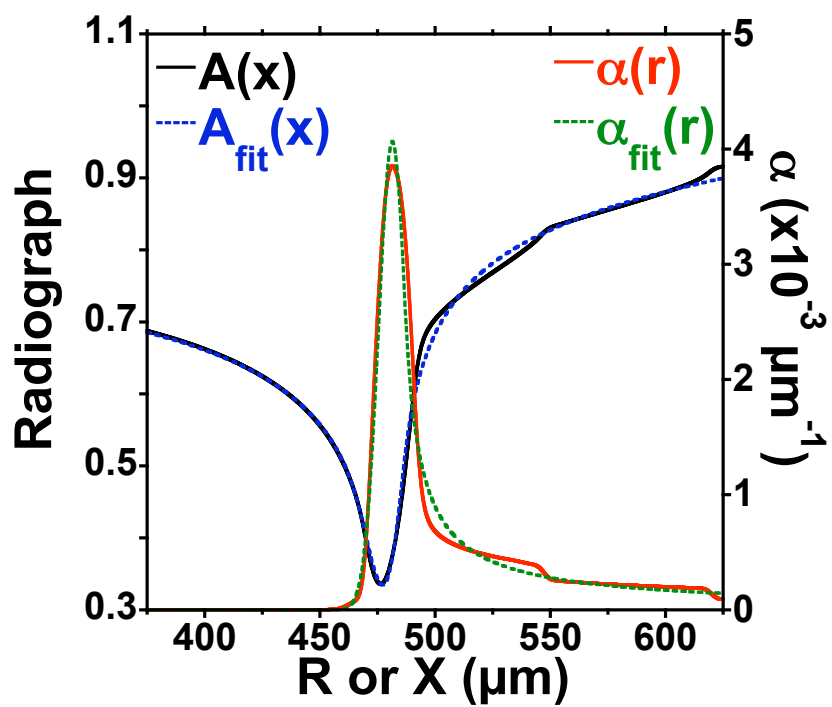


Figure 13

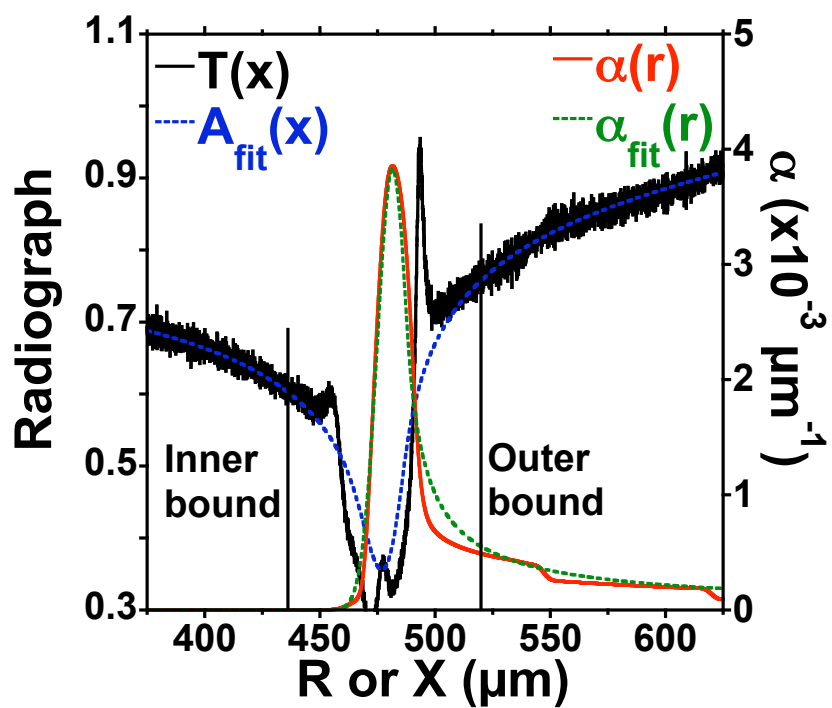


Figure 14

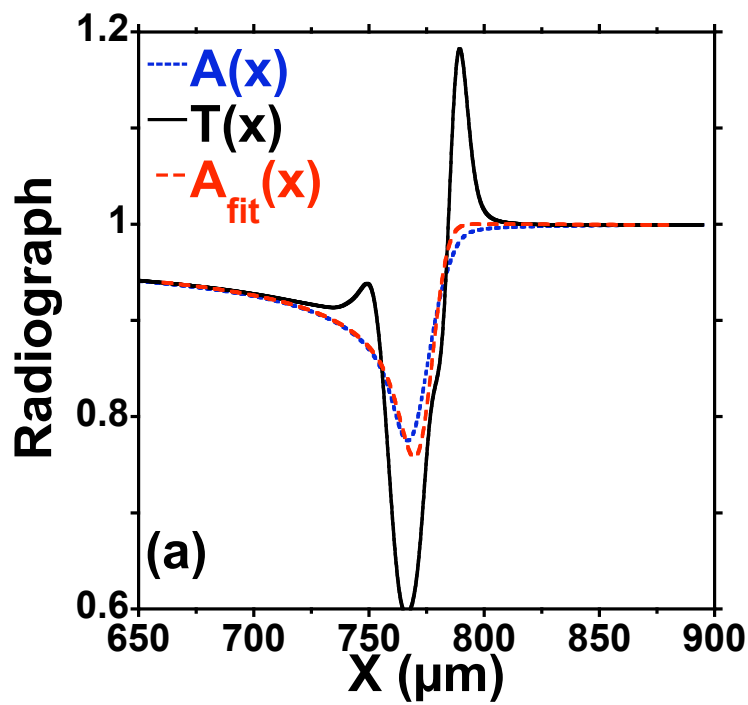


Figure 15(a)

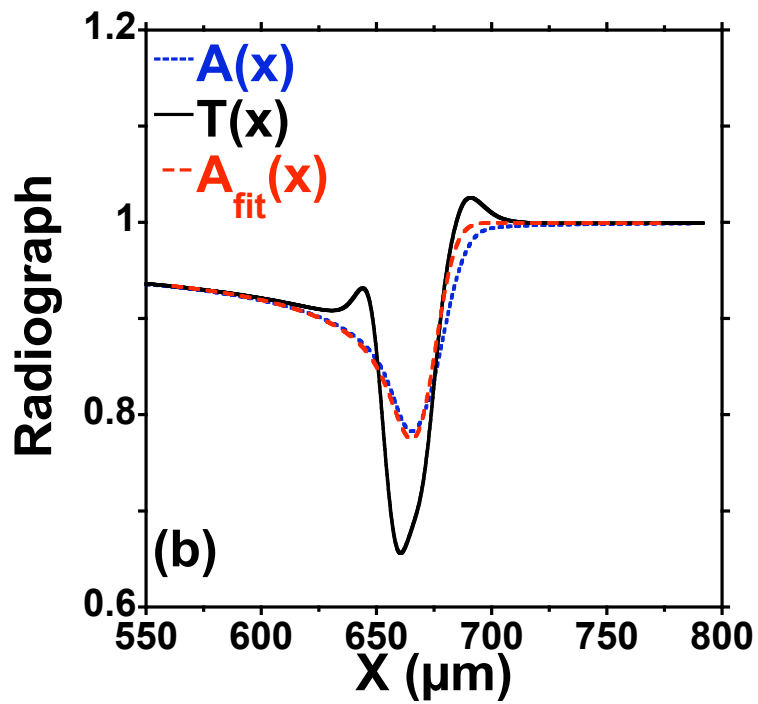


Figure 15(b)

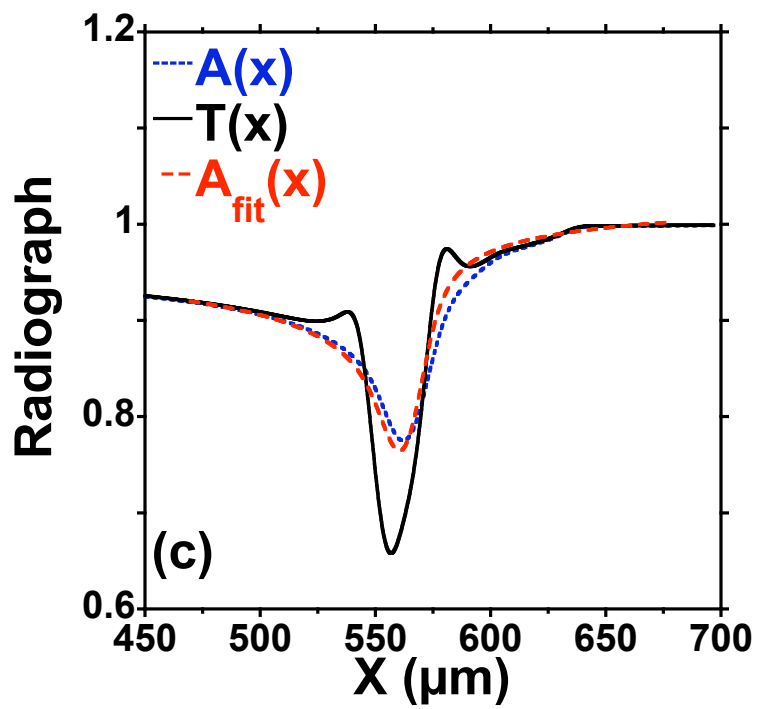


Figure 15(c)

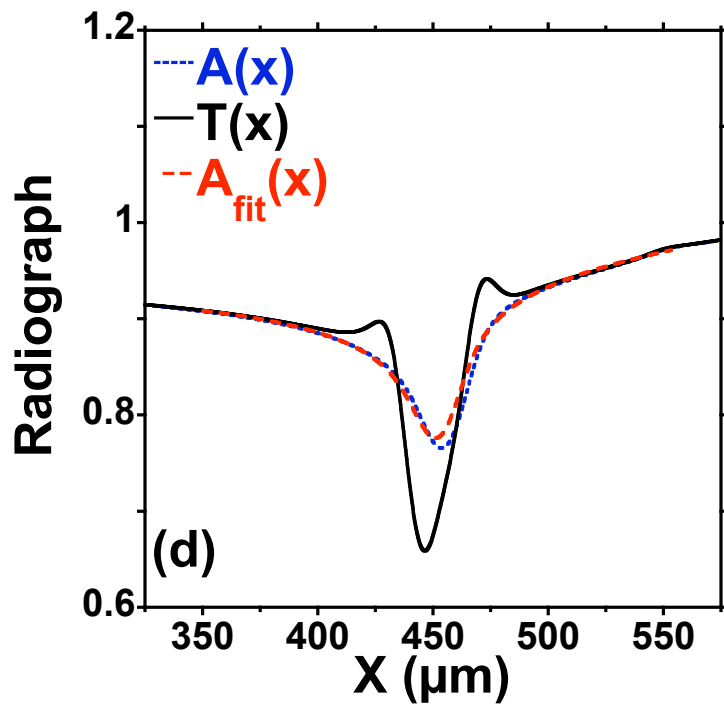


Figure 15(d)

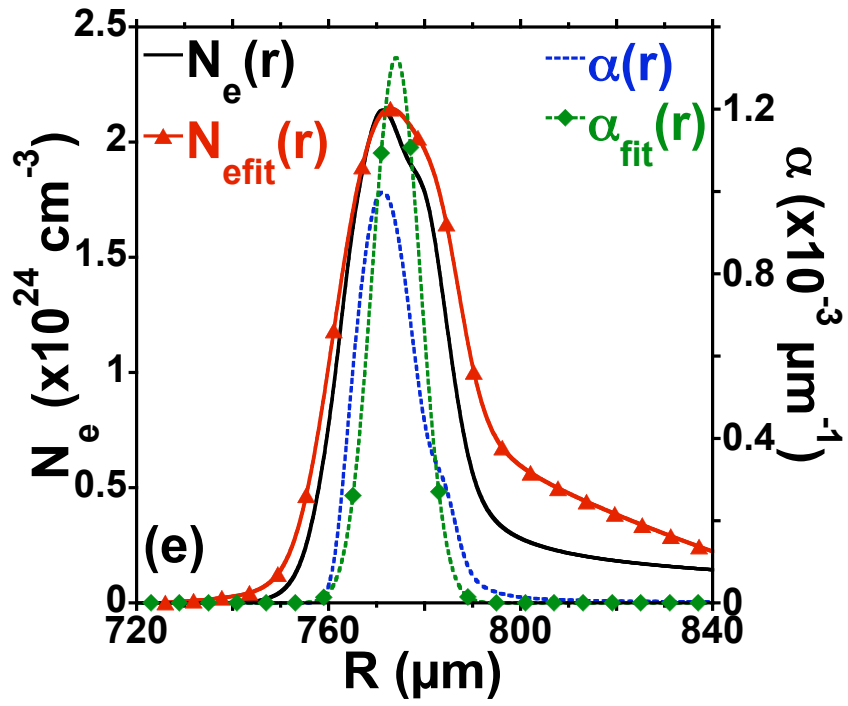


Figure 15(e)

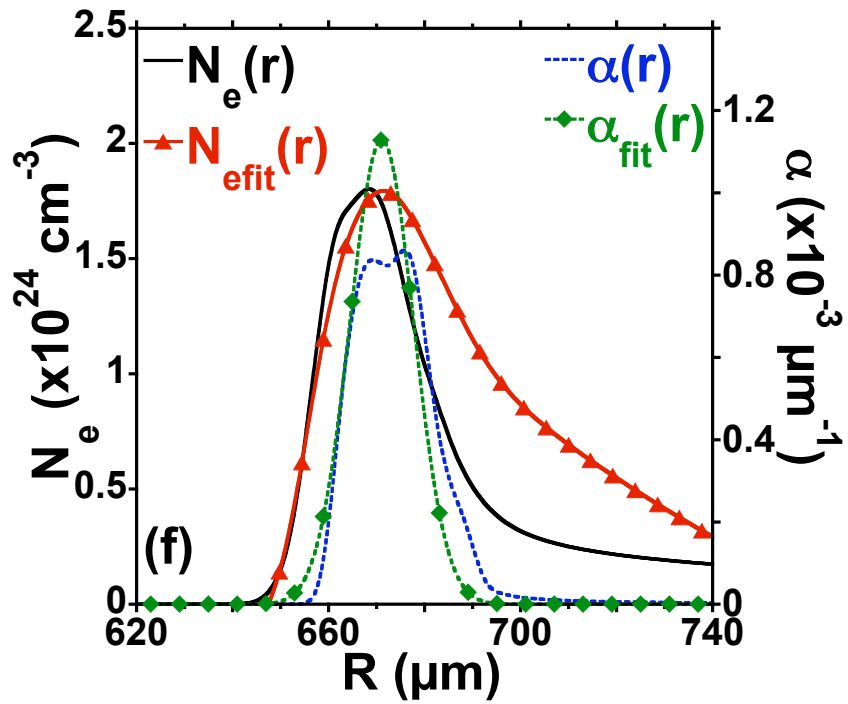


Figure 15(f)

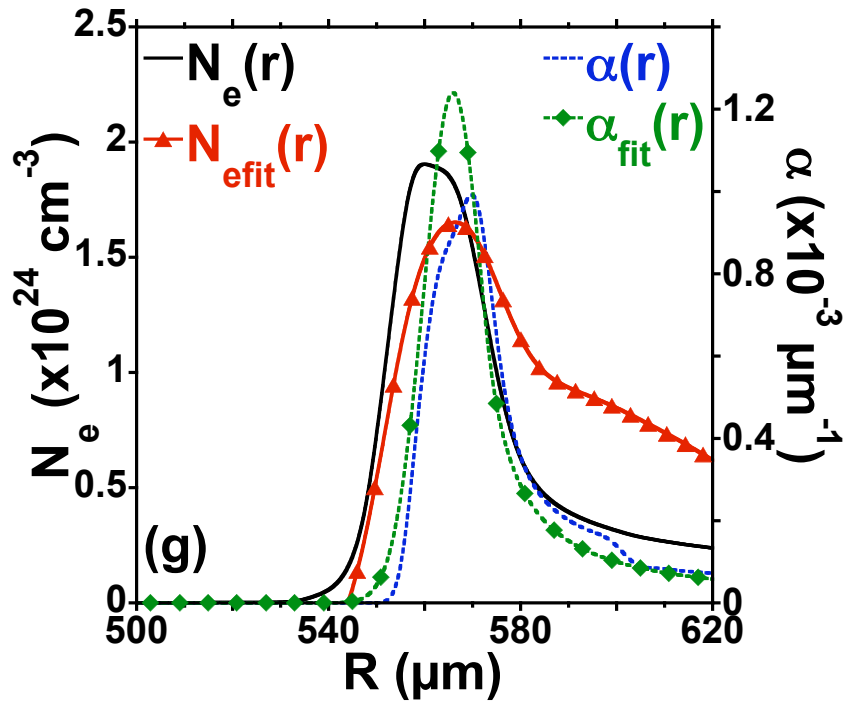


Figure 15(g)

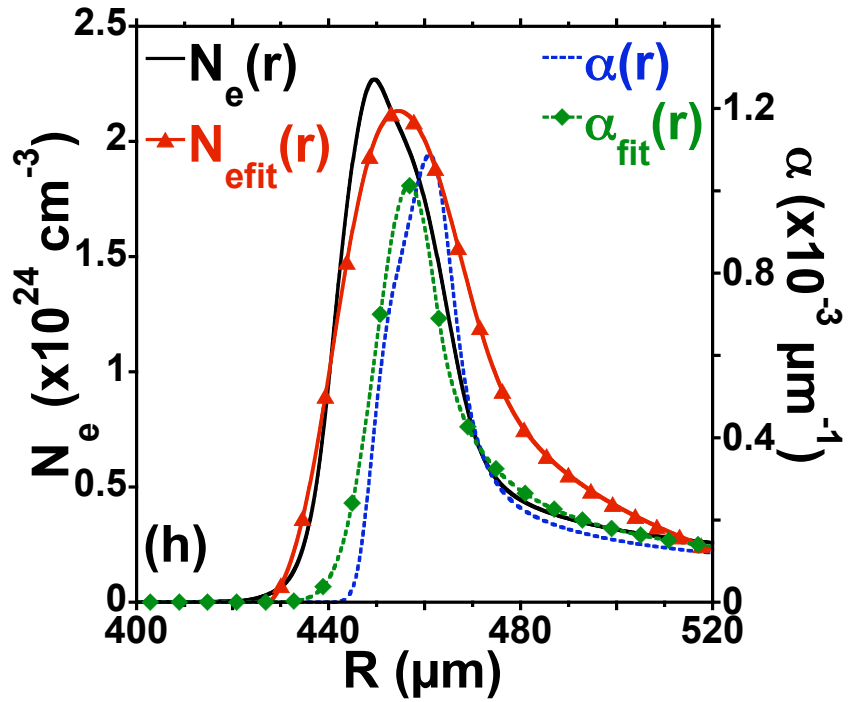


Figure 15(h)

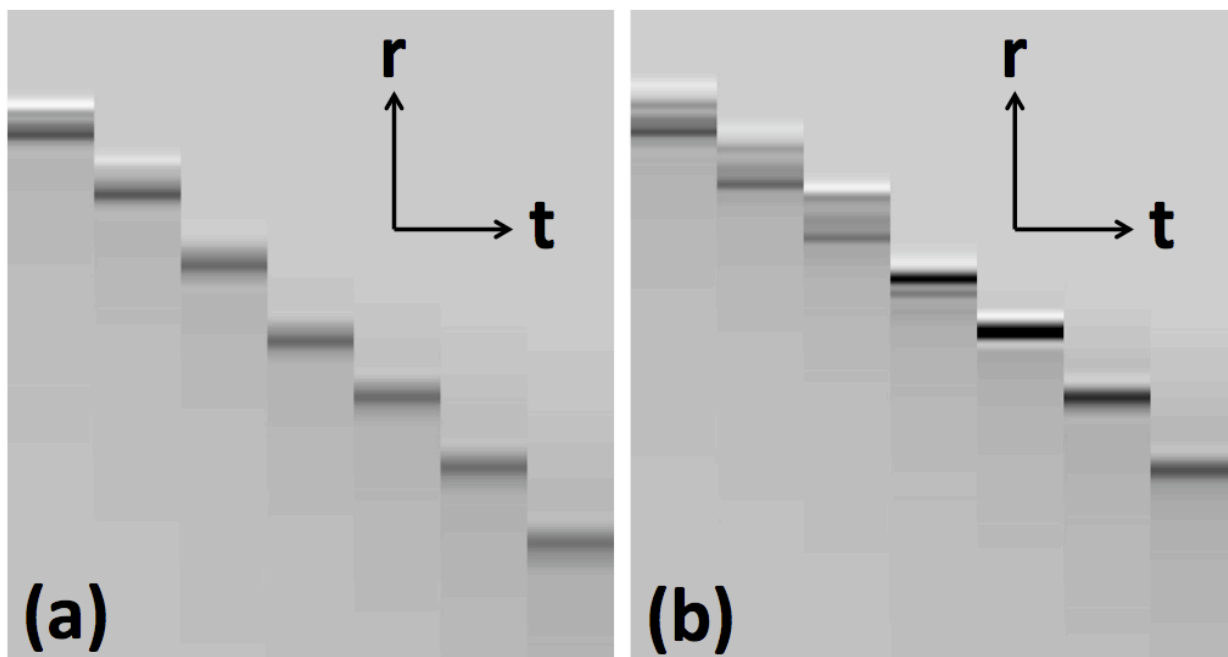


Figure 16

Table 1. Simulated and inferred parameters derived from refraction-enhanced radiograph analysis, at four different times during a simulated implosion.

Quantity	19.3 ns	19.9 ns	20.4 ns	20.8 ns
$N_e(r)$ width (μm)	33.1	34.3	30.2	31.7
Inferred $N_e(r)$ width (μm)	36.6	42.7	36.5	40.2
Error, $N_e(r)$ width	+ 3.5 μm	+ 8.3 μm	+ 6.2 μm	+ 8.5 μm
$\alpha(r)$ width (μm)	27.5	33.8	21.5	22.0
Inferred $\alpha(r)$ width (μm)	17.3	23.2	17.7	18.2
Error, $\alpha(r)$ width	- 10.2 μm	- 10.6 μm	- 3.8 μm	- 3.8 μm
r_{peak} of $N_e(r)$ (μm)	771.4	668.5	560.0	449.5
Inferred r_{peak} of $N_e(r)$ (μm)	772.9	671.5	566.3	454.6
Error, r_{peak} of $N_e(r)$	+ 1.6 μm	+ 3.0 μm	+ 6.2 μm	+ 5.1 μm
r_{peak} of $\alpha(r)$ (μm)	771.4	672.3	570.0	461.0
Inferred r_{peak} of $\alpha(r)$ (μm)	774.1	671.0	566.0	456.7
Error, r_{peak} of $\alpha(r)$	+ 2.8 μm	- 1.3 μm	- 4.0 μm	- 4.3 μm
Peak $N_e(r)$ ($\times 10^{24} \text{ cm}^{-3}$)	2.14	1.80	1.90	2.27
Inferred peak $N_e(r)$ ($\times 10^{24} \text{ cm}^{-3}$)	2.15	1.79	1.65	2.13
Error, peak $N_e(r)$	+ 0.3 %	- 0.4 %	- 13.2 %	- 6.0 %
Integral of $\alpha(r)r^2dr$ (μm^2)	9825	8649	7614	5945
Inferred integral of $\alpha(r)r^2dr$ (μm^2)	9930	8480	8007	6325
Error, integral of $\alpha(r)r^2dr$	+ 1.1 %	- 1.9 %	+ 5.1 %	+ 6.4 %